Chair of Materials Physics

Master's Thesis

Investigation of the crystallization behavior of iron-based metallic glasses for electrical devices

Felix Josef Römer, BSc

May 2022

MONTANUNIVERSITÄT LEOBEN
www.unileoben.ac.at

EIDESSTATTLICHE ERKLÄRUNG

Ich erkläre an Eides statt, dass ich diese Arbeit selbständig verfasst, andere als die angegebenen Quellen und Hilfsmittel nicht benutzt, und mich auch sonst keiner unerlaubten Hilfsmittel bedient habe.

Ich erkläre, dass ich die Richtlinien des Senats der Montanuniversität Leoben zu "Gute wissenschaftliche Praxis" gelesen, verstanden und befolgt habe.

Weiters erkläre ich, dass die elektronische und gedruckte Version der eingereichten wissenschaftlichen Abschlussarbeit formal und inhaltlich identisch sind.

Datum 23.05.2022

Unterschrift Verfasser/in
Felix Josef Römer

Contents

Index of Abbreviations

AM	*Additive Manufacturing*
bcc	*body-centered cubic*
BMG	*Bulk Metallic Glasses*
CHT	*Continous Heating Transformation*
DMD	*Direct Metal Deposition*
DSC	*Differential Scanning Calorimetry*
EBM	*Electron Beam Melting*
fcc	*face-centered cubic*
FDSC	*Fast Differential Scanning Calorimetry*
GFA	*Glass Forming Ability*
hcp	*hexagonal close-packed*
IM	*Injection Molding*
MS	*Melt Spinning*
RSP	*Rapid Solidification Process*
SLM	*Selective Laser Melting*
TTT	*Time Temperature Transformation*
XRD	*X-Ray Diffraction*

1. Introduction

The ongoing environmental crisis requires a significant reduction in power consumption. Amorphous core transformers have proven to reduce losses in transformers significantly. Hysteresis and eddy current losses are the two major types of losses. On the one hand, hysteresis losses reflect how easy it is to change the magnetic orientation. On the other hand, Eddy currents are losses due to the inductive generation of a current inside the material. Reducing these losses can be very beneficial in reaching climate goals. There are commercially available amorphous FeSiB system alloys [1]. However, due to their low saturation flux density and high magnetostriction, they need to be bigger and produce more noise than normal FeSi grain-oriented steels [2,3]. An optimal transformer material also needs to have an excellent glass-forming ability to be produced in significant amounts and consistent quality.

Metallic Glasses are of great interest due to their superior properties such as high hardness, high fracture strength, resistance to corrosion, and magnetic properties. Usually, the term “Glass” refers to amorphous oxides mostly made of silica and oxides of metals like Al, Mg, and Ca. Glasses are produced by cooling a molten mixture of silica and metal oxides very fast to avoid crystallization and “freeze” the random atomic structure of the liquid. Glasses are usually tough, brittle, often transparent and are used as window glasses, optics, and tableware.

When a metal is cooled down from its liquid state, the atoms arrange in specific crystalline order, such as body-centered cubic (bcc), face-centered cubic (fcc), or hexagonal close-packed (hcp). By cooling the melt very fast, the rearrangement of the atoms into three-dimensional structures can be prevented. As this solid has the atomic arrangement of the liquid, it is called a “Super-cooled Metallic Liquid” or a “Metallic Glass”. These Metallic Glasses build a whole new spectrum of materials. They can be used as they are or converted to a less metastable state to achieve the required properties. However, their large-scale use is prevented by the process-related dimensions in order to reach high enough cooling rates to build fully amorphous parts.

Various rapid solidification (RSP) techniques can produce metallic glasses, like melt spinning (MS), injection molding (IM), and additive manufacturing (AM). All these methods have different parameters for glass formation. Due to the necessity of high cooling rates of around 10^6 Ks^{-1}, the geometry of metallic glasses was limited to thin ribbons, foils, and powders. Increasing the alloying elements reduces the critical cooling rate and makes it possible to produce rods with diameters in the millimeter range. Nowadays, the glass-forming ability (GFA) of some alloys is so high that they can produce metallic glasses with critical cooling rates comparable to the cooling rates present in additive manufacturing methods like selective laser melting (SLM). This opens the third dimension and makes the production of near-net-shape, significantly bigger glassy parts possible without losing the exciting properties. Also, the layer by layer building of a part, therefore the subsequent heating and cooling of specific regions, can be used to crystallize certain phases and tailor the properties as desired.

In this thesis, two master alloys were prepared, namely $Fe_{74}Mo_4P_{10}C_{7.5}B_{2.5}Si_2$ and $Fe_{60}Co_{15}Ni_5P_{13}C_7$. Ribbons were prepared by melt spinning under a vacuum and high purity argon atmosphere. To prove amorphicity, the ribbons were analyzed by X-ray diffraction (XRD) and differential scanning calorimetry (DSC). Multiple heat treatments were developed, and the crystalization was analyzed utilizing XRD. Continuous heating transformation (CHT) Diagrams were produced by fast differential scanning calorimetry (FDSC), capable of cooling rates up to 50000 Ks^{-1}. This thesis aims to provide an enhanced understanding of crystallization during targeted isothermal annealing processes to control mechanical and magnetic properties.

2. Theoretical Foundations of Metallic Glasses

2.1. Metallic Glasses

When a metal is cooled down from its liquid stage, the atoms arrange in specific crystalline order, such as bcc or fcc. In nature, metals and alloys are generally considered crystalline, as their atoms are arranged regularly and periodically. By cooling the melt very fast, the rearrangement of the atoms into three-dimensional structures can be prevented. As this solid has the atomic arrangement of the liquid, it is called a "Super-cooled Metallic Liquid" or a "Metallic Glass" [4]. Figure 1 compares the atomic structure of single-crystalline, polycrystalline, and amorphous materials. Subsequently, it is conceivable to say that the atomic arrangement in the glass is similar to that of a fluid with the same composition [5]. A glass is classified as a material with no crystalline order because it lacks long-range periodicity and translational symmetry, and its constituent atoms are arranged randomly [6]. Traditionally metallic glasses are divided into the metal-metal type and metal-metalloid type. Metall-metalloid type metallic glasses usually have a metal content of 80%. The rest is made up of metalloids like P, B, or C. Metal-metal types typically have no restrictions on the content distribution. All Fe-based metallic glasses are of the metal-metalloid type [7–10]. This leads to relatively complex compositions but lowers the price of metallic glass as the metalloids are relatively cheap [11].

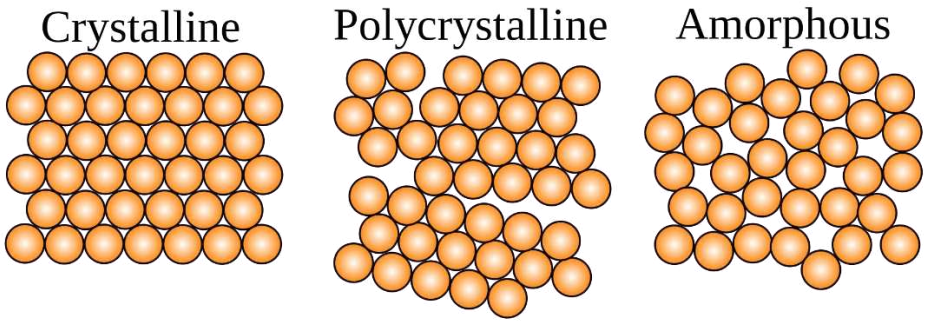

Figure 1: Comparison of the atomic arrangement of single-crystalline (perfectly ordered), polycrystalline (with grain boundaries), and amorphous materials (fully disordered) [12].

Even though they have excellent strength, Fe-based metallic glasses are not used in structural applications as they behave very brittle under mechanical loading. Much work has been done to enhance ductility by introducing microstructural heterogeneities like separated phases, nanocrystals, and atomic clusters by adding small amounts of soft elements [11]. Understanding the effects of alloying elements on the mechanical, electrical, and thermal properties is crucial for designing metallic glasses with tailored properties.

2.1.1. Synthesis of Metallic Glasses

The first metallic glasses were synthesized by Pol Duwez et al. in 1960 by using the so-called gun technique [13]. In this process, a small amount of melt is propelled onto a thermally conducting substrate, resulting in a spread-out thin foil with cooling rates of 10^5 - 10^6 Ks^{-1}. The possibility of forming a glass varies from cooling rates of 1 $Kmin^{-1}$ for some oxide-based blends (through a high number of components) to the necessity of very high cooling rates of 10^{10} Ks^{-1} for monoatomic metals [14]. Because of these high cooling rates, the geometries are mostly restricted to thin foils, powders, and ribbons. To accomplish such high cooling rates, all rapid solidification processes rely on bringing the melt in close contact with a highly conducting surface with a relatively high heat capacity at a high velocity [15]. In the last 40 years, many new multicomponent systems with low critical cooling rates have been discovered. In order to produce “Bulk metallic glasses” (BMG), alloy design principles based on atomic mismatch, chemical interaction, and phase diagram considerations have been developed. Metallic glasses with a critical casting thickness of at least 1 mm can be called BMG. The possibility of producing normally crystalline material in an amorphous state led to the development of various other techniques [16].

2.1.1.1. Melt Spinning

Melt spinning has been the most common technique for producing metallic glasses since it was introduced by Duwez et al. in 1960 [13]. In the melt spinning process, a molten metal jet is directed onto a cold, thermally highly conductive wheel that spins at high frequencies. An induction coil melts the metal. The molten metal gets jetted by a pressure difference between the main chamber and the pressure chamber. When the metal touches the spinning wheel, it quickly solidifies with a cooling rate of 10^6 Ks^{-1}. By this technique, long ribbons with a thickness of several tenths of a micrometer can be produced. The thickness depends on the wheel's rotational speed and the applied pressure. At the same time, the width can be changed by a bigger or smaller diameter of the crucible's tip. Figure 2 shows a schematic of the melt spinning method.

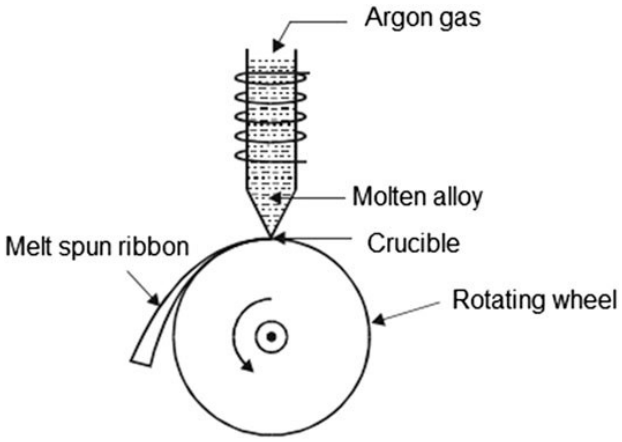

Figure 2: Schematic of the melt spinning method [17].

2.1.1.2. Additive Manufacturing

Because of the limiting factors of the high cooling rate and the limitation of crystallization, it is generally hard to produce complex amorphous structures. Additive manufacturing methods like SLM [18–22], direct metal deposition (DMD) [18], electron beam melting (EBM) [18], and laser foil printing LFP [23] can overcome this issue by relatively high cooling rates during the "layer-by-layer" process. This makes it possible to surpass the dimensional limits of BMGs, which has drawn much attention in recent years [7,20,22,24]. Figure 3 shows a schematic of the SLM process. The cooling rates can reach 10^4 – 10^8 Ks^{-1} [19,25], which is higher than the necessary cooling rates of most metallic glasses. During the SLM process, a layer of powder is applied to a thermally conductive base plate. A laser melts the necessary contours, and the powder quickly solidifies into an amorphous solid. The base gets lowered, and the process is repeated until a whole part is built.

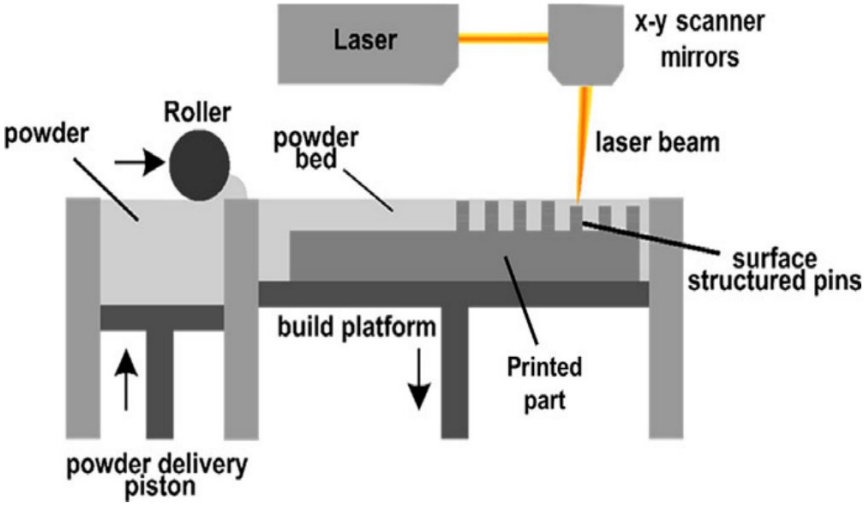

Figure 3: Schematic of the SLM process [18].

Many parameters can influence the SLM process, as shown in Figure 4.

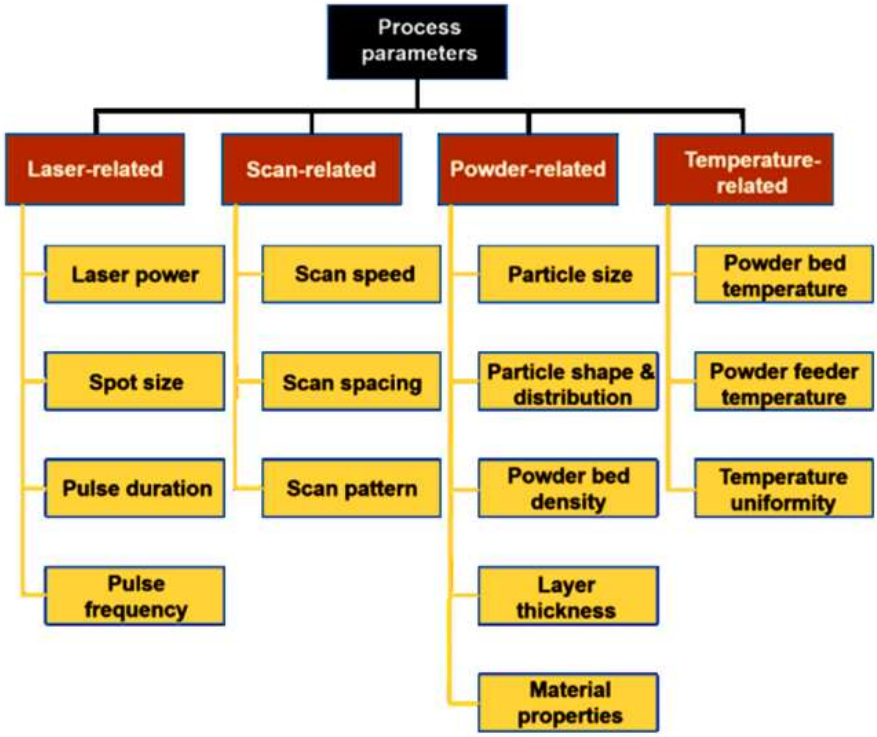

Figure 4: Control parameters of the SLM process [18].

2.1.2. Glass Formation

Usually, when a melt is cooled down in equilibrium, the atoms arrange in a specific crystalline order. In order to form an amorphous phase, the free energy has to be lower than the free energy of the corresponding crystalline phases. The Gibbs free energy is calculated by:

$$G = H - TS \quad (1)$$

Free energy reduction is possible by increasing the entropy of fusion ΔS_f or decreasing the enthalpy of fusion ΔH_f, or both. It is easy to increase ΔS_f by increasing the number of components in a system. The increase in ΔS_f also leads to an increase in dense random packing of atoms, decreasing ΔH_f and increasing the solid-liquid interfacial energy. Both of these factors lead to a reduction of free energy.

2.1.2.1. Glass Forming Ability

The glass forming ability (GFA) is the ability of a crystalline metallic alloy to transform into a glassy state. Structural and kinetic parameters determine the GFA of alloys [26]. Structural criteria consider the geometric arrangement of atoms, bonding, and atomic size. Kinetic criteria evaluate the cooling rate in relation to the crystallization kinetics. Both structural and kinetic criteria are essential, but the structural parameters seem to be the most important in determining the GFA [27].

2.1.2.2. Critical Cooling Rate

To avoid the nucleation and development of observable crystal fractions in quenching molten alloys, bulky glass formation in metallic systems demands a modest cooling rate. As a result, the critical cooling rate is regarded as a reliable reference for determining the GFA of BMGs. A low critical cooling rate indicates an easy glass formation. The critical cooling rate can be obtained from the TTT Diagram by:

$$R_c = \frac{T_m - T_n}{t_n} \quad (2)$$

Here T_m is the melting temperature, and T_n is the temperature of the "nose" point at which t_n time is needed to start crystallization. Unfortunately, this equation overestimates R_c because it assumes that the crystalization rate corresponds to the "nose" of the TTT curve throughout the whole temperature range T_m to T_n [26,28].

The Barandian-Colmenero expression [29] can be used to calculate the critical cooling rate.

$$ln\,R = lnR_c - \frac{b}{(T_l - T_{xc})^2} \qquad 3$$

R_c is the critical cooling rate, b the material constant, T_l the liquidus temperature, and T_{xc} the onset solidification temperature of the melt at a cooling rate of R.

2.1.2.3. Effects of Alloying Elements

Alloying elements can be divided into atoms with positive and negative enthalpy of mixing. If elements with a negative enthalpy of mixing are added to the main constituent, the effect on the GFA is strongly dependent on their atom size.

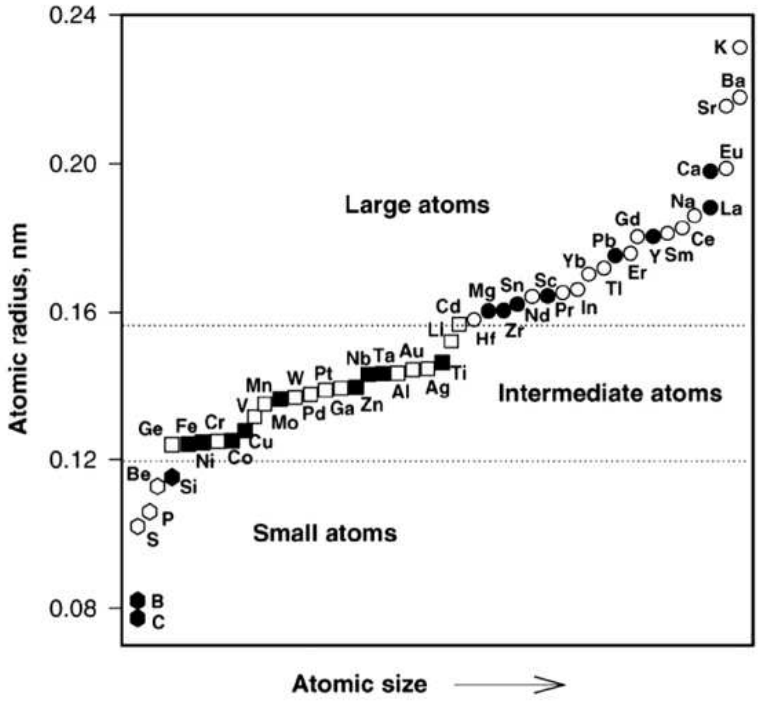

Figure 5: Atomic radii of possible microalloying elements for BMGs [30].

Figure 5 shows that the smallest elements for alloying BMGs are C, B, S, P, Be, and Si. C, B, Si, and P have been studied the most due to their significant impact on the GFA. Only very few glass formers have been developed without these elements [6,31]. In order to suppress crystallization, thermodynamic and kinetic consideration have to be made. From the thermodynamic point of view, the driving force of glass formation $-\Delta H^{amor}$ and the resistance against crystallization $\Delta H^{amor} - \Delta H^{inter}$ have to be considered. Figure 6 shows the contribution of the metalloid content to the driving force of glass formation and resistance against crystallization. Carbon contributes the most to stabilizing the amorphous phase for alloys with a single metalloid [32]. From the kinetic point of view, the viscosity is strongly related to the GFA. In order to crystalize, the atoms have to experience a high degree of reordering. All super-cooled liquids exhibit increasing viscosity when cooled down under T_g [33]. Therefore, the crystallization process takes significantly more time in a viscous fluid. The maximum critical size for Fe-BMGs has reached 16 mm by miner alloying of Yttrium [34].

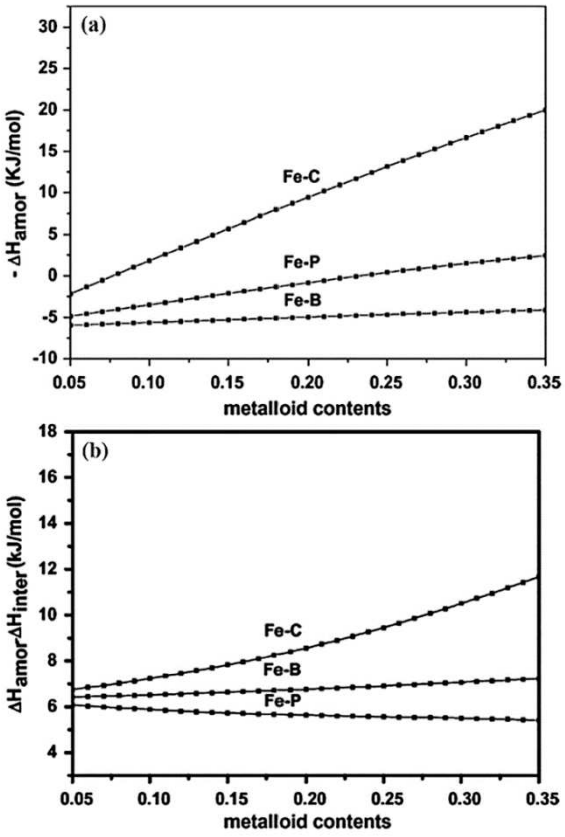

Figure 6: Effects of metalloid elements addition in Fe-based BMGs a) on the driving force of glass formation and b) on the resistance against crystallization [32].

2.1.2.4. Reduced Glass Transition Temperature

When a melt is cooled down from the liquid state, its viscosity increases. The glass transition is defined as the temperature where the viscosity reaches 10^{12} Pa·s. Turnbull [35] suggested that the ratio between the glass transition temperature T_g and the liquidus temperature T_l should be a good indicator of an alloy's glass-forming ability. The reduced glass transition temperature $T_{rg}=T_g/T_l$, where T_g is the glass transition temperature, and T_l is the endset of the endothermic melting peak, has often been cited in the literature as a critical parameter determining the glass-forming ability of metallic glasses. High values of T_{rg} are associated with high viscosity and good glass-forming ability. The high values of T_{rg} indicate a small temperature range for which crystal nucleation and growth can occur [36]. Turnbull suggested, based on the nucleation theory, that at $T_{rg} > 2/3$, homogenous nucleation of the crystalline phase is entirely suppressed. Typically a minimum of $T_{rg} \approx 0.4$ is necessary to form a glassy alloy.

Focusing on the T_{rg} value, the glass-forming ability can be improved by lowering the liquidus temperature. For example, in deep eutectic alloys, the melting point is lower than the individual components. The melting point strongly decreases with higher solute content until a minimum is reached at the eutectic composition. At the eutectic point, the liquid phase is thermodynamically preferred over the solid phase because the crystalline phases are destabilized, or the liquid state is stabilized [6]. Furthermore, the driving force for nucleation and growth of crystalline phases below the eutectic temperature at the eutectic composition is rather low. Crystallization of the liquid requires a significant rearrangement of the various atoms to generate new phases, so the glass formation is kinetically favored at the eutectic composition. Accordingly, there also T_{rg} is very high. This connection was often exploited in the early development of metallic glasses [6].

2.1.2.5. Egami and Waseda

A possibility to enhance the glass-forming ability is to introduce lattice strain by adding significantly bigger or smaller atoms. The lattice strain disturbs the crystal lattice and destabilizes the crystal. Using the atomic scale elasticity theory, Egami and Waseda [37] calculated the atomic stresses in the solid solution. They observed that local stress fluctuations and total stain energy normalized to the elastic moduli do not vary significantly with solute concentration. However, the strain energy was observed to increase linearly with solute content. This indicates that when a critical solute concentration is reached, the glass becomes energetically more favorable than the crystalline phase. It was found that the minimum solute concentration C_b^{min} in binary solutions is inversely correlated with the atomic mismatch $(V_A-V_B)/V_A$, where V_A is the atomic volume of the solvent and V_B is the atomic volume of the solute.

$$\left|\frac{(V_A - V_B)}{V_A}\right| C_B^{min} = 0.1 \qquad 4$$

2.1.2.6. Inoue Criteria

Based on the synthesis of many bulk metallic glasses, Inoue [38–40] formulated three basic rules for the formation of metallic glasses:

- The formation of glass becomes easier with an increasing number of elements. In order to form a glass, an alloy has to contain a least three elements.
- The atomic mismatch between the main constituent elements must be as big as possible. A mismatch above 12% is suggested.
- The participating elements should have a negative heat of mixing.

2.1.2.7. Δq-GFA

Li et al. [41] used a new approach to quantifying the glass-forming ability. They used a data-driven approach and analyzed 5727 alloys by producing them by magnetron sputtering and x-ray diffraction. They found a correlation between the full-width half maximum of the amorphous peak and the glass-forming ability of numerous systems. The key to comparing the different alloys is in the same production procedure. The characterization in the XRD can reveal if the alloy is glassy or crystalline. They interpreted Δq (L = 2π/Δq) to reflect the degree of structural ordering in the metallic glass. A larger Δq corresponds to a shorter correlation length L, and thus the ordering can only be maintained over short distances, indicating a more disordered structure. In order to compare different alloy systems, the correlation length L is normalized by the weighted average atomic diameters. They state that this approach is around 250 times more effective than conventional strategies.

2.1.2.8. CCT Diagrams

Figure 7 shows a schematic of a continuous cooling transformation (CCT) Diagram. Crystallization is indicated by the intersection of the cooling curve R_{cryst} with the crystal region “nose”. This typical “nose” comes from the competition between the driving force for nucleation and atomic mobility. At high temperatures, the atomic mobility is high due to diffusion, whereas the driving force for nucleation is low due to low undercooling. The critical cooling rate is the minimal colling rate at which no crystallization and only vitrification occur. The formation of a fully amorphous phase is only possible if the cooling rate of the process is at least as high as the critical cooling rate, provided the alloy is cooled below the glass transition temperature T_g without any changes in the liquid. Cooling down faster as the critical cooling rate suppresses the crystallization and leaves the system in a non-equilibrium condition. To vitrify, the system has to fulfill specific requirements: the alloy has to possess a low driving force for crystallization [42], and structural relaxation should be lowed down to suppress atomic arrangement [35,43,44]. These parameters shift the crystallization “nose” to longer times, leading to a lower critical cooling rate. Depending on the exact composition, the critical cooling rate is in the order of 10^2 – 10^6 Ks^{-1}.

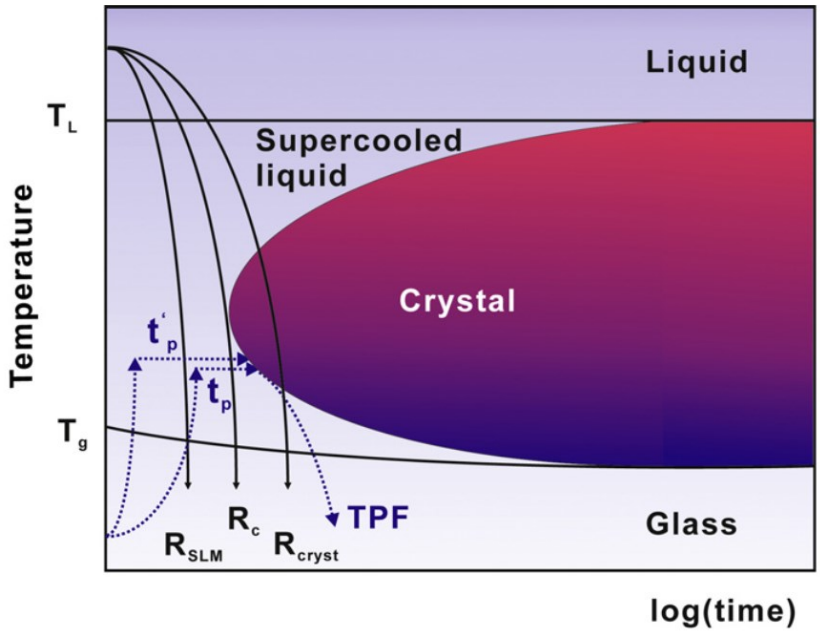

Figure 7: Schematic of a CCT diagram [21].

As the system is in a non-equilibrium condition, it tends to lower its energy by crystallization. The C shape of the curve represents that at any given temperature, the minimum time required to form a stable solid phase. The processing has to occur above T_g and before crystallization T_x to process

metallic glasses and keep the amorphous structure. Above T_g, the viscosity rapidly decreases [35,45], enabling thermoplastic deformation indicated by the dotted line in Figure 7 [33,46]. The deformation has to be finished in a relatively short time t_p before crystallization occurs. The faster the part is heated, the longer is the processing window, as indicated by t_p'. With rising heating rates, the crystallization temperature is shifted to higher temperatures. At the critical heating rate, the heating rate is high enough to entirely suppress crystallization when heating the glass into its liquid state [47]. The critical heating rate is usually two magnitudes higher than the critical cooling rate [48].

2.1.3. Crystallization of Metallic Glasses

After its formation, the glass is in a highly non-equilibrium state. When heated over its glass transition temperature, the atoms rearrange to reach a more stable state. Upon annealing under the glass transition, the glass slowly becomes an "ideal" glass of low energy by structural relaxation. Relaxation is a characteristic of metallic glasses due to their far-from-equilibrium state and is closely related to atomic diffusion, rearrangement of nearest atoms, and nanoscale heterogeneities [49,50]. Every glass possesses defects, generally considered free volume, but the amount depends on the production parameters. This free volume is annihilated upon annealing resulting in a denser material [6]. Isothermal annealing below glass transition reduces residual stresses [30,51] and improves soft magnetic properties [52]. Understanding the micromechanisms of crystallization is crucial for impeding or controlling crystallization. This is necessary for potential applications, as the stability against crystallization determines their application limits.

Crystallization usually occurs as a result of nucleation and growth processes in order to reduce the free energy. Usually, crystal nucleation has to happen before growth [53]. The number density of nucleation centers N influences the rate of crystallization. The density of nucleation centers is insensitive to the heating rate, as it saturates upon heating. The temperature dependence of growth is predominant over nucleation [53]. Figure 8 shows the Fe-B system's hypothetical free energy diagram for the stable α-iron and Fe_2B phases and the metastable Fe_3B and amorphous phase. The solid tangential line shows the equilibrium coexistence of α-iron and Fe_2B. The dashed lines show possible metastable equilibria. The transition of the metastable amorphous phases into the crystalline phase can occur by one of the following reactions:

a. Polymorphous crystallization

   This reaction is only possible if the concentration is near the pure elements or compounds. The amorphous alloy crystallizes into a supersaturated alloy or a stable or metastable crystalline compound without any changes in concentration [54].

b. Primary crystallization

During the crystallization of one phase, e.g., α-iron, the amorphous phase is enriched in boron until a metastable equilibrium stops the crystallization. A concentration gradient is produced at the crystallization front. For further crystallization to happen, more atoms have to diffuse through the depleted surrounding of the crystallization front, which decreases the growth rate. Further crystallization happens much slower due to Ostwald ripening. The radii r of spherical crystals follow a parabolic relationship with respect to the annealing time t,

$$r = \alpha\sqrt{D * t}, \qquad 5$$

where D is the diffusion coefficient, and α is a dimensionless parameter dependent on the concentration on the interface and the sample's composition. The dispersed crystalline phase can act as nucleation sites for the following crystallization [54].

c. Eutectic crystallization

A eutectic crystallization is the simultaneous crystallization of two crystalline phases by a discontinuous reaction [54]. In the reaction front, the two phases separate, which is generally slower than the two other processes. Because the separation only occurs directly on the reaction front, there is no change in composition in the surrounding amorphous material.

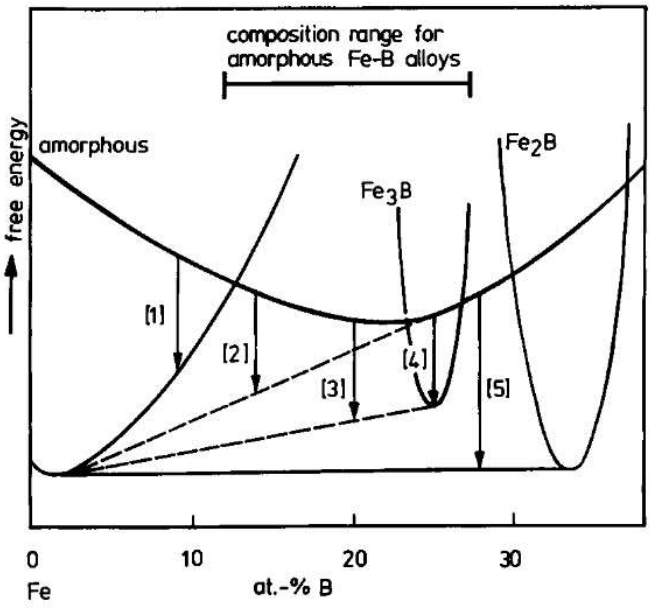

Figure 8: Hypothetical diagram of the free energy in the Fe-B system [54].

The Kissinger method is an effective way to determine the crystalization energy E for the first crystallization peak [55]. The Kissinger equation can be written as:

$$E = -R\frac{dln(\frac{\beta}{T_p^2})}{dT_p^{-1}} \qquad 6$$

R is the ideal gas constant, β is the heating rate, and T_p is the peak temperature of the first crystallization. This indicates that the activation energy can be derived as the slope of the Kissinger plot when $\ln\left(\frac{\beta}{T_p^{-1}}\right)$ is plotted over $\frac{1}{T_p}$. Although very easy, the Kissinger method makes some assumptions by simplifying the thermally stimulated process. It oversimplifies the crystallization as it yields a single value of the activation energy, regardless of the complexity [56]. Because these processes are commonly multi-step [56], the temperature dependence cannot be described by single activation energy. It also does not account for thermal inertia, as it is estimated that this term can be neglected [57]. By not accounting for this, the peaks in the DSC may appear to be at higher temperatures as they should, which can lead to a systematic error in the value of the activation energy. This error decreases with lower mass and a slower heating rate. The International Confederation of Thermal Analysis and Calorimetry (ICTAC) recommends that the product of mass and heating rate should not exceed 100 mgK/min [58].

2.1.3.1. Devitrification

The unique properties of metallic glasses are expected to be destroyed by devitrification. Over the years, it has become apparent that totally or partially crystalline materials produced from metallic glasses might have valuable properties. Slight devitrification can be helpful in tailoring properties [59]. A fine dispersion of crystals in a ferromagnetic glass can pin domain boundaries and reduce hysteric losses at high frequencies [60]. Also, surface devitrification can induce stresses and change magnetic anisotropy [61]. Another possibility is to enhance mechanical properties by fully devitrifying the metallic glass. The critical point is that a crystalline material made of metallic glass has a very fine and uniform microstructure. As devitrification is essentially solidifying a liquid at very high undercooling, crystal nucleation is favored over crystal growth, resulting in a very fine microstructure [59]. The first significant application of a devitrified alloy was the hard magnetic alloy $Fe_{14}Nd_2B$ [62].

Table 1: Enhanced properties by devitrification [59].

Property	Reference
Mechanical properties	
Increased ductility	[63]
Increased flow stress and fracture strength	[64,65]
Superplasticity	[66]
Increased hardness	[67,68]
Soft magnetic properties	
Low coercivity	[69–71]
High saturation magnetization	[69–71]
Reduced high-frequency losses	[72]
Stress-induced anisotropy	[61]
Hard magnetic properties	[62]
Increased critical current type II superconductors	[73]

Recent work from Tong et al. investigated the underlying structural origins of the enhanced soft magnetic properties by devitrification of $Fe_{76}Si_9B_{10}P_5$ [71]. They found that separate and dense coordinated Fe-metalloid atomic clusters are formed in the short-range order, strengthening the ferromagnetic exchange interaction (Figure 9). In the medium-range order, creating homogeneous Fe-M clusters and the residual matrix with configurational stabilization is encouraged to generate coupled homogeneous strong and weak ferromagnetic regions, which help the domain wall move and rotate by weakening the heterogeneity of the coupling energy.

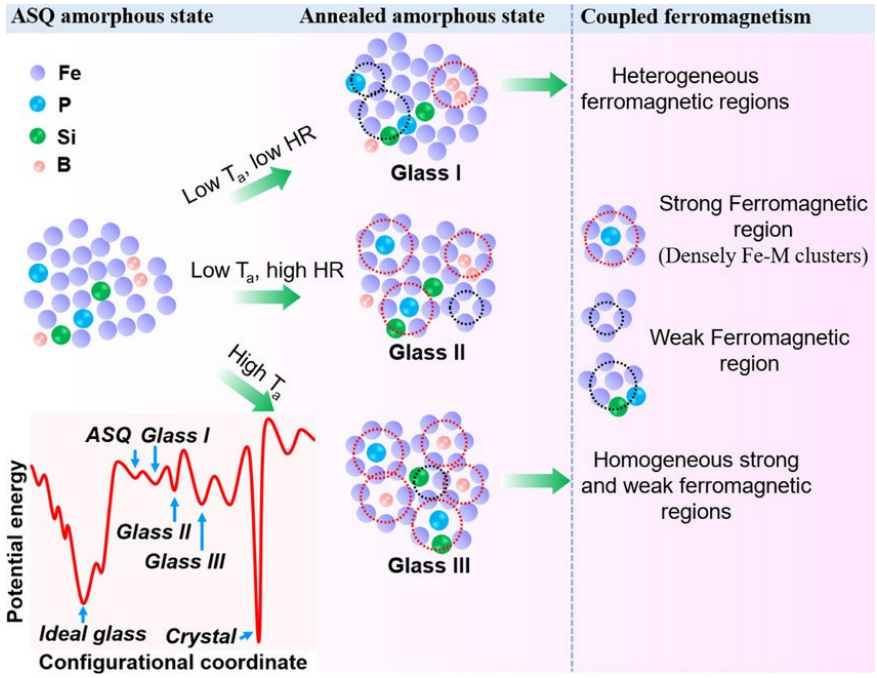

Figure 9: Structural evolution of $Fe_{76}Si_9B_{10}P_5$ alloy during various isothermal annealing processes [71].

To achieve uniform microstructure, the annealing temperature and the heating rate play essential roles in Fe-based metallic glasses [74,75]. Previous work has shown that optimal soft magnetic properties can be achieved by annealing at ~$0.96 \cdot T_g$ [3].

2.1.4. Soft Magnetic Properties

BMGs are of particular interest because of their excellent soft magnetic properties [3,6,43,52,76–78], such as high saturation magnetization, low coercivity, and high electrical resistivity. Because of the need for BMGs for a good GFA, some sacrifices must be made. For example, alloying raises the GFA but lowers the saturation magnetization. It has been found that the maximum possible amount of Fe is required for the highest possible saturation magnetization [6]. Annealing the amorphous alloy between the Curie temperature T_c and the crystallization temperature T_x has been shown to impact soft magnetic properties significantly. These alloys are based on the precipitation of α-Fe during annealing. Therefore the crystallization must happen at least in two stages. The annealed alloys have been found to have much better magnetic properties than in their fully amorphous state [6]. The Herzer model [79] suggests that when the exchange-correlation length is in the order of the grain size D, the magnetic properties are strongly enhanced

by averaging the magnet-crystalline anisotropies over multiple domains. Thus, the sample exhibits minimal resistance to coherent domain rotation by an external field. Figure 10 shows that the precipitation of very small crystalline grains significantly lowers the coercivity. Due to the low coercivity, low core losses, and low material costs, soft-magnetic ribbons such as FINEMET [80], NANOPERM [81], and HITPERM [82] have been widely used as transformers, motors, and other electric components.

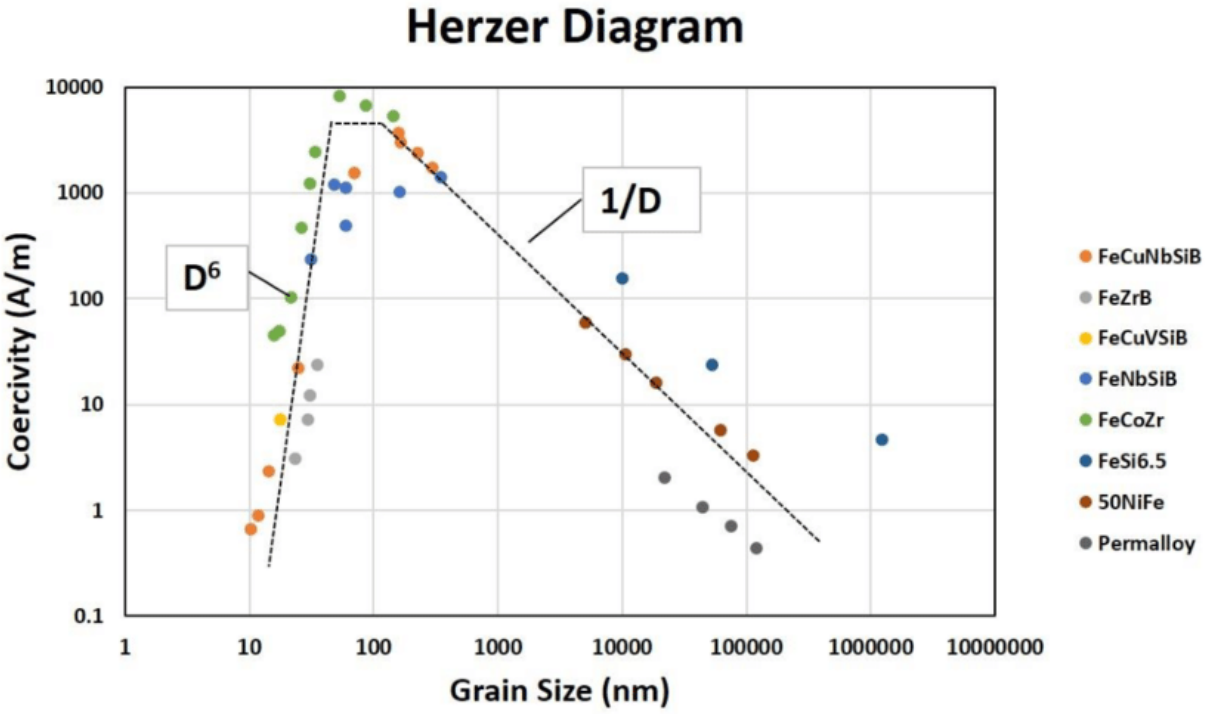

Figure 10: Herzer Diagram showing the dependence of the grain size on the coercivity [79].

3. Experimental

This part describes the techniques used to obtain the as-cast metallic glass ribbon, perform the heat treatment, and characterize the samples.

3.1. Sample Preparation

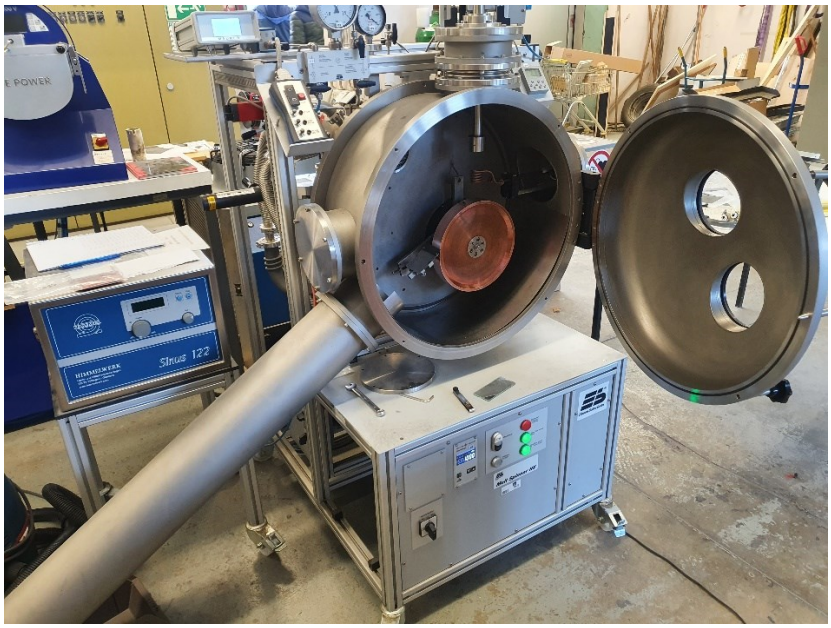

Figure 11: Picture of the melt-spinning setup used in this work.

The ribbons were prepared using a Melt Spinner HV from Edmund Bühler GmbH (Germany) (Figure 11). Figure 12 shows that the crucible's opening must be polished until the tip has an opening of 1 mm.

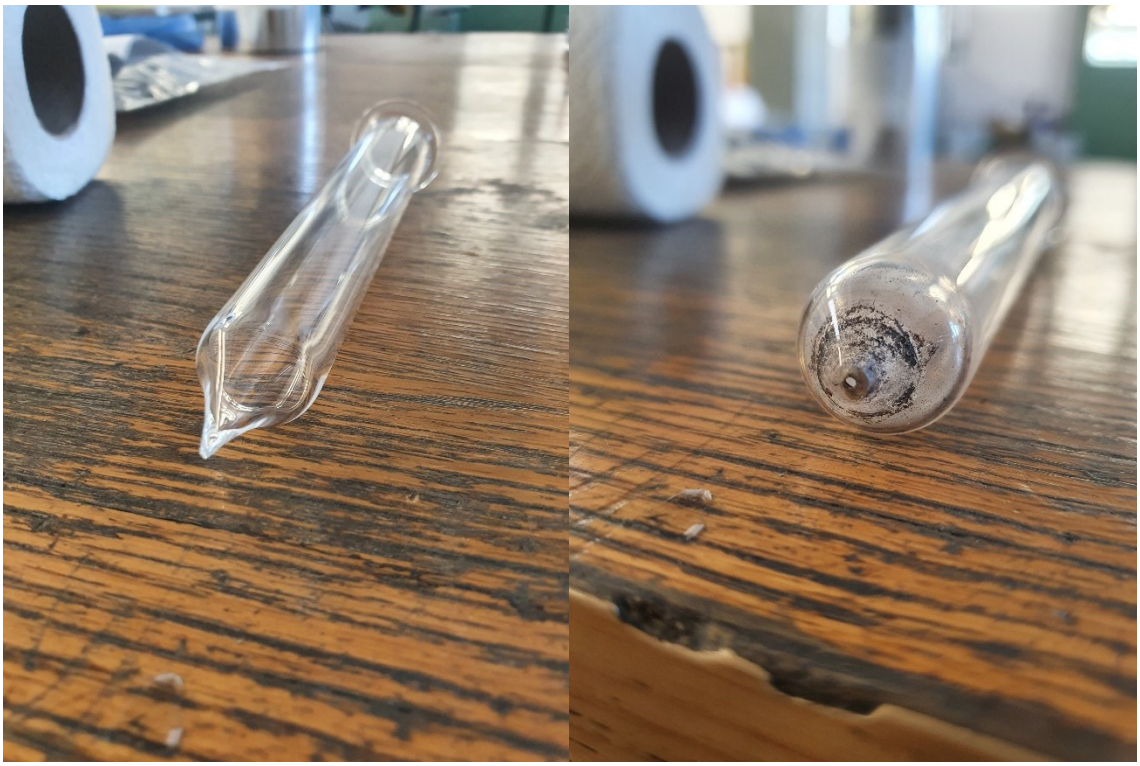

Figure 12: Picture of the unused and the used crucible.

Around 3.5 – 4 g of material are put into the crucible and mounted into the vacuum chamber. All experiments were performed under 400 mbar Argon atmosphere after vacuuming the pressure chamber twice to $1.5 \cdot 10^{-2}$ mbar. The valves for the main chamber are closed, and the pressure chamber is filled with additional argon until the desired pressure difference of 400 mbar is reached. Then the crucible with the material is placed inside the induction coil to ensure good heating. An optical sensor controls the temperature accurately. The high-frequency generator is turned on, and the current is gradually increased until the material is melted and the desired temperature is reached. Then the molten material is released onto a rotating copper wheel by pressing a button. The wheel was turning at a specific frequency, and with the diameter of the wheel, the speed can be calculated. The ribbons fall off the copper wheel and are collected in a separate tube-shaped chamber.

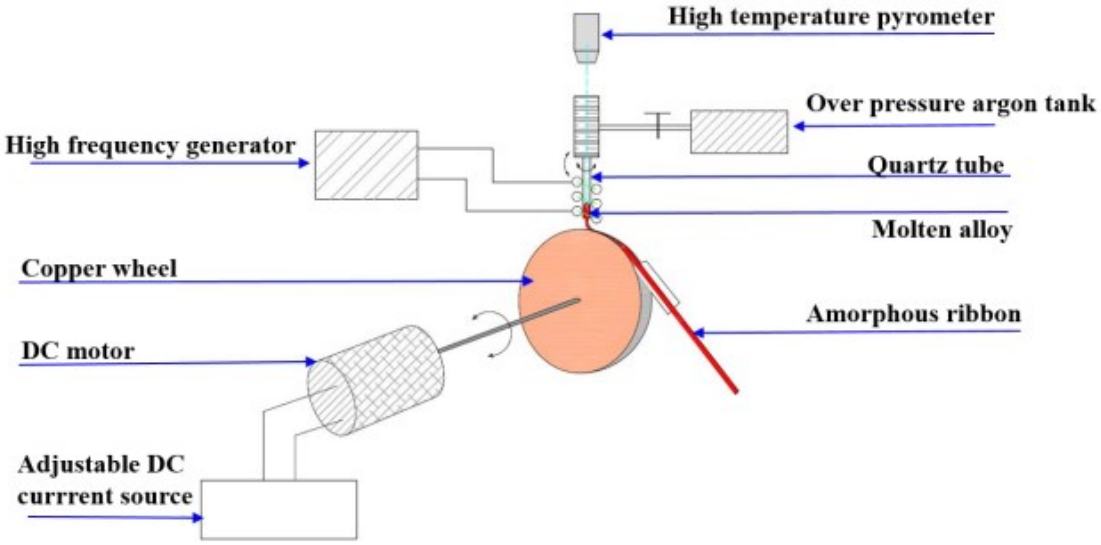

Figure 13: Schematic illustration of a melt spinning setup [83].

3.2. DSC Measurements

Differential scanning calorimetry is a thermal analysis device that measures how the physical properties change over time during heating or cooling. Calorimeters are frequently used in chemistry, biotechnology, and material science to assess the thermodynamic properties of materials. DSCs are divided into two types based on their operating mechanism: heat-flux DSCs and power-compensated DSCs. In a heat flux DSC, the sample material is enclosed beside an empty reference pan. Both pans are heated simultaneously in the sample chamber under the same conditions. The furnace is heated at a linear heating rate, and the heat is transferred through a thermoelectric disk [84,85]. The sample's heat capacity leads to a temperature difference between the sample and the reference pans. Thermocouples measure this temperature difference, and the consequent heat flow is determined by:

$$q = \Delta T / R \qquad 7$$

Where q is the sample heat flow, ΔT is the temperature difference between sample and reference, and R is the resistance of the thermoelectric disk.

In a power-compensated DSC, the two pans are placed in separate furnaces. The thermal power necessary to keep the sample and the reference at the same temperature is plotted over time or temperature [85].

DSC measurements were performed on a DSC 404 F1 Pegasus from Netsch (Germany). This DSC is of the heat flux type and is capable of temperatures between 123 K and 1473 K with heating and cooling rates of 0.001 $Kmin^{-1}$ to 50 $Kmin^{-1}$. The sensitivity and temperature were calibrated for the heating rates 5, 20, and 50 $Kmin^{-1}$ using In, Bi, Zn, Ag, and Au by comparing the measured heat flow with reference values. First, the sample crucible and the reference crucible are carefully weighted. To prevent the sticking of molten material to the wall, a layer of Y_2O_3 is added and weight onto the bottom of the crucible. A sample of approximately 10 mg was carefully weight and placed inside the ZrO_2 crucible. Before the experiment, the chamber was vacuumed and flushed two times with argon. The glass transition temperature T_g, the crystallization temperature T_x and the melting temperature T_m were measured using the onset temperature of the related peaks.

3.3. FDSC Measurements

Ordinary DSC measurements are limited to a few Ks^{-1}. In contrast, Flash DSC instruments are capable of cooling rates between 0.1 and 50000 Ks^{-1}. The Flash DSC measurements were performed on a Flash DSC 2+ from Mettler Toledo (Ohio, US) with an intracooler TC100-MT from Huber Kältemaschinenbau AG (Germany). The Flash DSC 2+ is of the power compensated type. The sensor chips were high-temperature chips UFH 1 for temperatures up to 1273 K from Mettler Toledo. According to the manual of the Flash DSC 2+, the chips were conditioned and thermocouple corrected. Before every experiment, the chip was measured empty to obtain a baseline. Then a small sample between 5 ng and several micrograms was prepared, scraping it off the ribbon using a scalpel. The ideal sample should fit within the boundaries of the sensor membrane and be as thin and flat as possible to ensure excellent thermal contact.

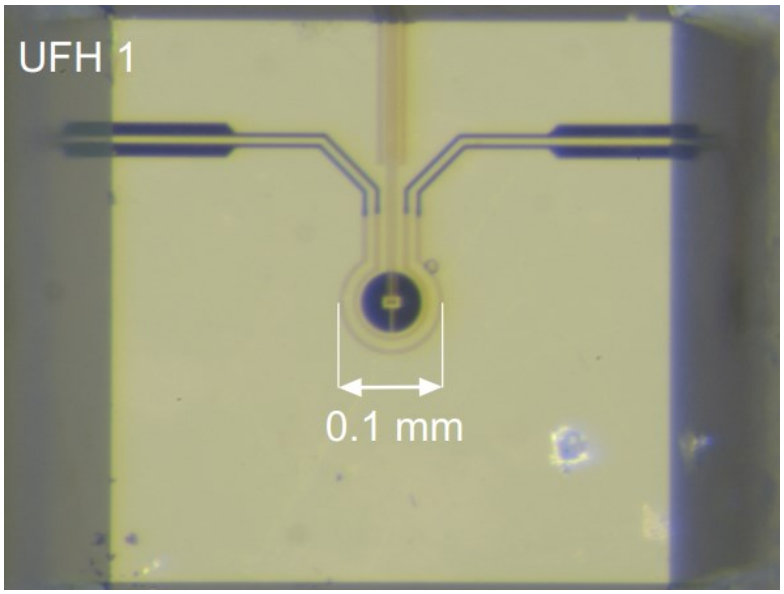

Figure 14: Sample area of the UFH 1 chip sensor membrane [86].

It was then transferred to the chip sensor by an electrostatic manipulator. After the sample was placed in the middle of the membrane, the insulation lid was closed, and the Argon gas valve was opened. In order to avoid any oxidation, the Argon gas flow was set to the maximum possible value of >80 ml/min and was maintained for several minutes before starting the experiment. The tests were performed with different heating rates to obtain CHT Diagrams.

3.4. XRD Measurements

XRD is a powerful method that provides information on regular 3-dimensional structures like crystals. It is used to determine crystal structures, lattice parameters, crystallinity, phase composition, and residual stresses. Bragg's law is the underlying equation of XRD methods:

$$n\lambda = 2dsin(\theta) \quad (8)$$

Where n is an integer, λ is the wavelength, d is the distance between diffracting planes, and θ is the incident angle. If Bragg's law is fulfilled, the X-ray beam interferes constructively with the crystal planes, and a peak is measured on a detector. The location of the peaks in crystalline structures indicates the distance between the periodic arrangement of structural units. The width indicates the correlation length between these units. In an amorphous material, the broad peaks indicate average atomic distances. To prove amorphicity, all samples were analyzed in their as-cast ribbon state by XRD. These analyses were performed in reflection configuration on a D2

phaser from Bruker (MA, USA)) with Co-K_α radiation (λ = 1.7089 Å) and Fe as the K_β filter. The diffraction patterns were recorded between 2θ = 20° and 120° with a step size of 0.02°. These 2θ are then converted into the wave vector q with equation 9.

$$q = \frac{4\pi}{\lambda * 10 * \sin\left(\frac{2\theta}{2}\right)} \quad 9$$

The samples were attached to the PEEK sample (Figure 15) holder using silicon oil to hold the samples in place.

Figure 15: Picture of the PEEK sample holder.

The sample holder and the silicon oil do not contribute to the XRD pattern. The ribbons have two sides. During production, one side faces the spinning wheel, and the other faces the atmosphere in the chamber. The ribbon is considered amorphous when the side facing the atmosphere is amorphous as the wheel's cooling rate is much higher, supporting glass formation.

Further experiments were conducted with annealed samples. They were exposed to an isothermal heat treatment according to their DSC curves. Several temperatures before and after each crystallization peak were selected. The heat treatments were performed in the high-temperature DSC under an argon atmosphere with a 20 $Kmin^{-1}$ heating/cooling rate and an isothermal holding time of 60 seconds.

3.5. In-situ SXRD

Synchrotron radiation is emitted when charged particles traveling at a speed close to the speed of light are forced into a curved trajectory by a magnetic field. Such radiation can have a wide energy range from infrared and ultraviolet to the x-ray region [87]. The radiation is produced in high-energy, electron, or positron circular accelerators. Figure 16 shows the schematic top view of a synchrotron facility. It is made of circular evacuated pipes with magnets positioned around the perimeter that cause electrons to follow circular trajectories. A linear accelerator increases the electrons to millions of electron volts (MeV). Then a booster ring accelerates the energy to giga electron volts (GeV). They are then transferred to the storage ring, where they may be further accelerated.

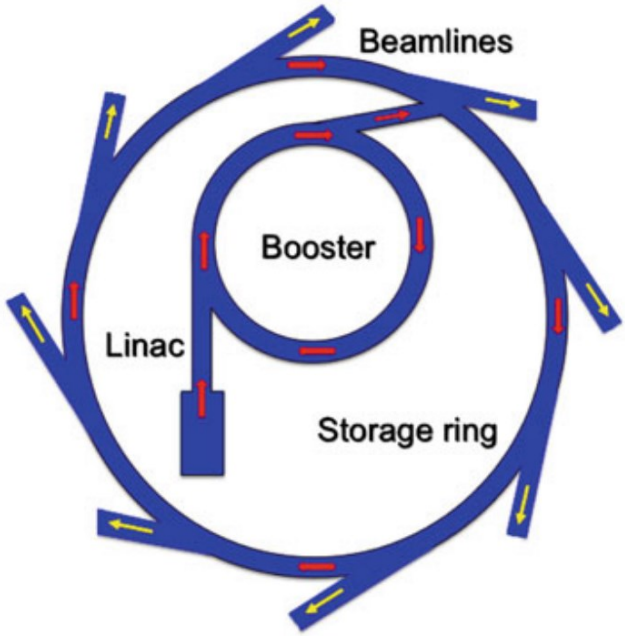

Figure 16: Schematic of a synchrotron radiation facility [87].

In each turn, the electrons lose energy in the form of synchrotron radiation. The energy loss is regained by passing through radiofrequency cavities. The beam produced in a synchrotron has the following main properties [87]:

- high intensity;
- very broad and continuous spectral range;
- natural narrow angular collimation;
- high degree of polarization;

- pulsed time structure;
- high brightness;
- high beam stability;
- ultra-high vacuum environment.

The SXRD measurements were performed in situ during Flash DSC experiment as described in 3.3 at the P21.2 Swedish Materials Science Beamline of the Petra III Synchrotron (DESY Hamburg). A Pilatus 3 2M detector from Dectris (Swiss) was used. The CdTe sensor is capable of detecting 250 frames per second and features a large sensitive area of 25 x 28 cm^2 filled with small pixels with a size of 172 x 172 μm^2. The measurements were performed by Mihai Stoica, Cameron Quick, and Florian Spieckermann with the support of the Beamline Scientists Zoltan Hegedusz, Timo Müller, and Ulrich Lienert.

3.5.1. Data Preparation

In the course of this master's thesis, a series of scripts were developed to support the evaluation of synchrotron experiments. The used language was Python 3 [88] and the essential packages were pyFAI [89] for the azimuthal integration, FabIO [90] to read the images, concurrent.futures [91] for multiprocessing, and Matplotlib [92] to display the results. The scrips are attached in the appendix.

3.5.1.1. Calibration

In order to measure valid data, the whole setup must be calibrated. This is usually done by measuring Debye-Scherrer rings collected from a reference powder. Multiple calibrants can be used, including ceria, corundum, gold, lanthanum hexaboride, and silicon [89]. The setup consists of a detector, the six refinement parameters like the distance, and fixed parameters like the wavelength. Provided the wavelength and energy are known, the reference aperture is calculated and saved on a text file with a ".poni" ending. The detector distance was 0.49 m, and the wavelength was $3.26 \cdot 10^{-11}$ m.

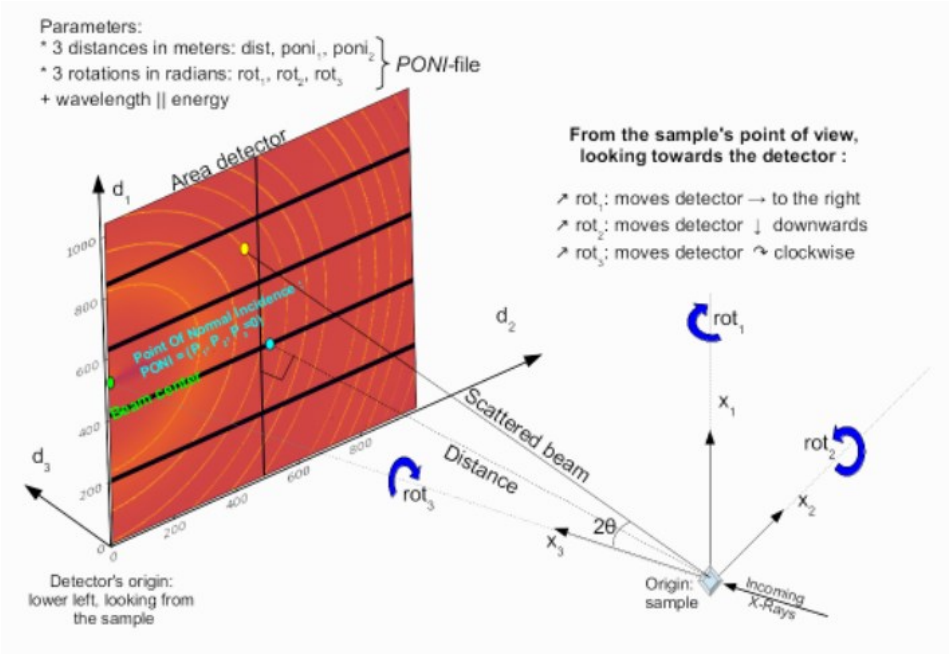

Figure 17: Geometry of the diffraction setup [93].

3.5.1.2. Integration

The data was collected on a Pilatus 3 2M detector from Dectris (Swiss). This is a 2D area detector with a large sensitive area of 25 x 28 cm^2 filled with small pixels with a size of 172 x 172 μm^2. The pictures are then converted into 1D curves, utilizing azimuthal integration. This step is normally the most time-consuming one. The software pyFAI was used to reduce the 2D data into 1D curves, further processed with a custom programmed scrip. Also, multiprocessing was implemented using the concurrent.futures library [91]. This reduced the integration time by around 35 times on a 40-core processor.

3.5.1.3. Masking

During the in-situ SXRD measurements, the specimen was mounted onto a chip with gold contacts. In order to separate the chip's peaks from the relevant data, a script was written in Python 3 [88]. Multiple measurements on the empty chip were performed at room temperature. The script averages these measurements and subtracts the background. Figure 18 shows the steps of the masking process. It can be seen that the mask was sufficient to mask all of the peaks at room temperature. It becomes harder to successfully mask the peaks at high temperatures as they shift to high q with rising temperature. This has to be taken into consideration when interpreting the evaluation of the XRD data. Insufficiently masked peaks suddenly appear at higher temperatures and vanish when cooled down at room temperature.

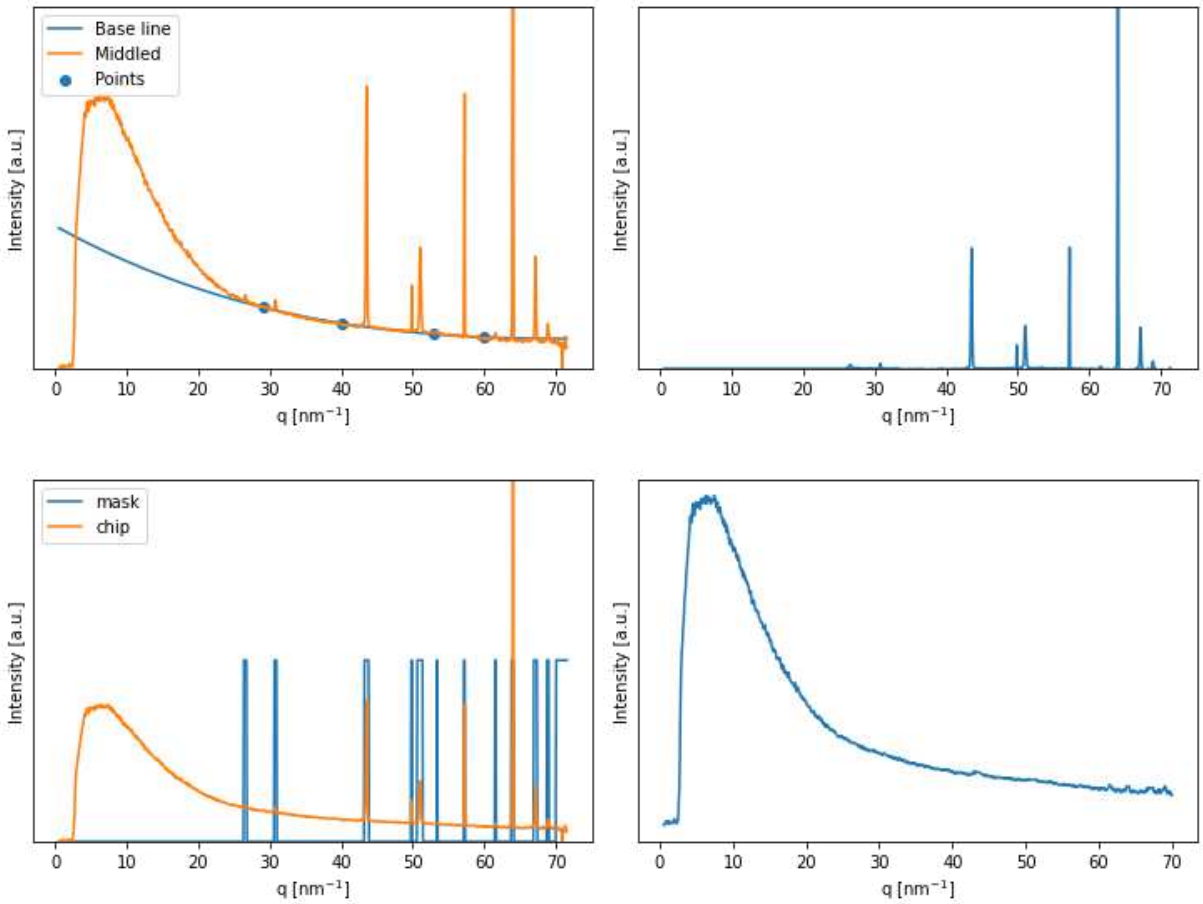

Figure 18: Measurement of the empty chip a) with background b) without background c) resulting mask and d) fully masked chip

3.5.1.4. Final Preparation

The final editing consists of the subtraction of the background as well as masking the chip's peak with the in chapter 3.5.1.3 created mask. After this final editing, the data is stored as .txt files, which are used to obtain an intensity map of the XRD data over the whole heating process.

3.5.1.5. Temperature Evaluation

Although the XRD data is measured simultaneously with the DSC data, the exact temperature cannot be derived. There is a lag between the start of the experiment and the start of the actual

heating. In order to take this into account, the chips peaks were observed in detail. Figure 19 shows that the wavevector q changes with rising temperature. This fact can be used to determine the exact frame in which the cooling starts. The exact temperature curve can be back-calculated with the knowledge of the start of the cooling phase. Thus every frame can be associated with the corresponding time and temperature.

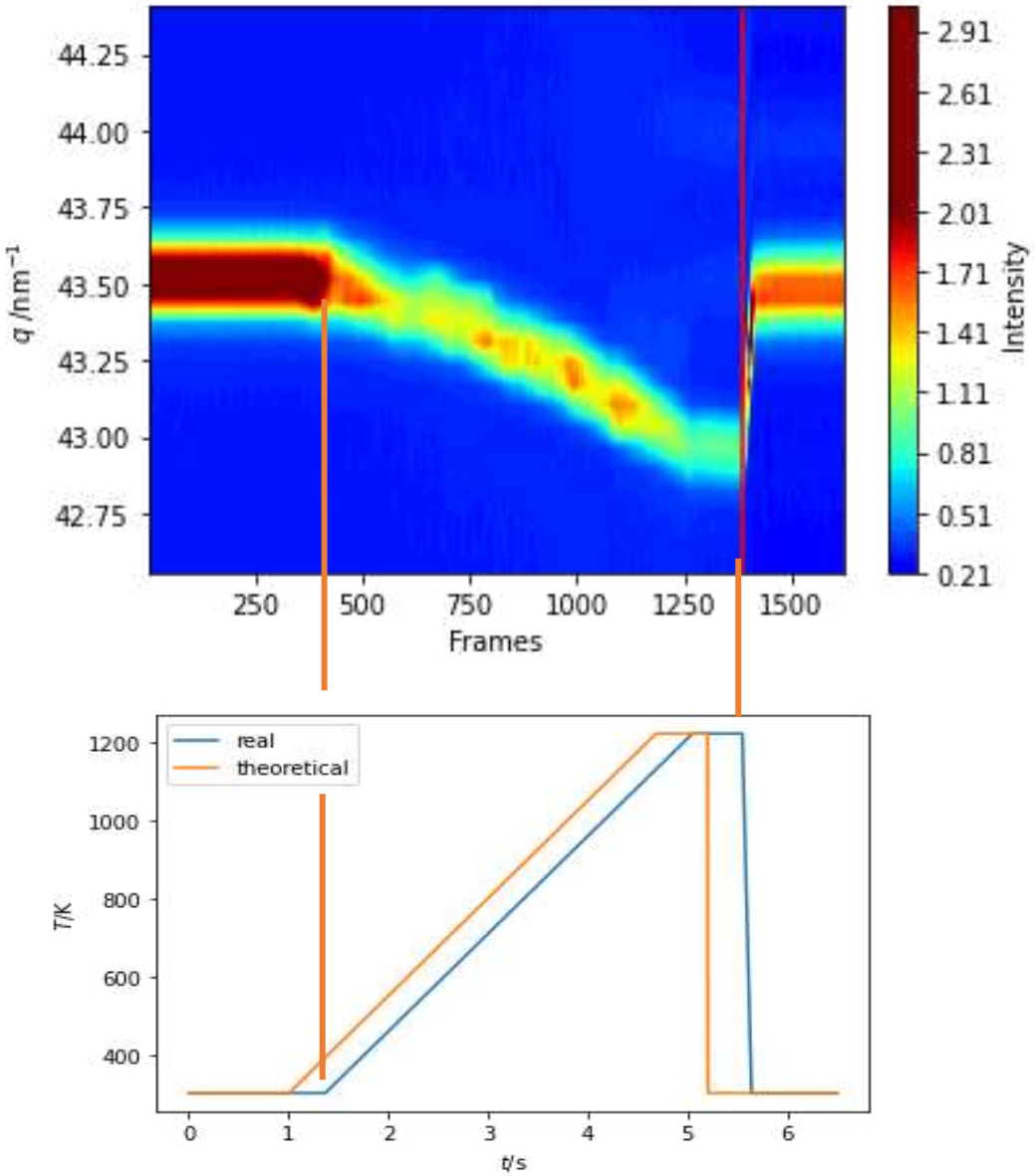

Figure 19: Temperature evaluation by observing the shift in q with rising temperature.

4. Results and Discussions

In this chapter, the results of the two alloys are presented.

4.1. $Fe_{60}Co_{15}Ni_5P_{13}C_7$

This alloy was prepared as a master alloy from industrial grade material and melt-spun at 1400 K under a high purity argon atmosphere (99% pure) as described in chapter 2.1.1.1. Since Fe-based alloy has a high affinity to oxygen and due to the low vacuum, contamination with oxygen is expected [4,6,9,94,95]. These oxides might induce heterogeneities that act as heterogeneous nucleation sites, resulting in a lower glass-forming ability. Figure 20 shows the high-temperature DSC curve at 20 $Kmin^{-1}$ of the as-cast ribbon. The alloy exhibits a glass transition at 673 ± 1 K and three crystallization peaks at 684 ± 1 K, 706 ± 1 K, and 732 ± 1 K. After that, there is an endothermic peak at 1053.65 K caused by the loss of the magnetic order at the Curie temperature. The endothermic peak at around 1175 ± 1 K indicates the α→γ phase transformation of iron. The alloy starts to melt at 1228 ± 1 K. The temperatures corresponding to the glass transition and the crystallization points, as well as ΔT_x and the reduced temperature, are measured as onset temperatures and are summarized in Table 2.

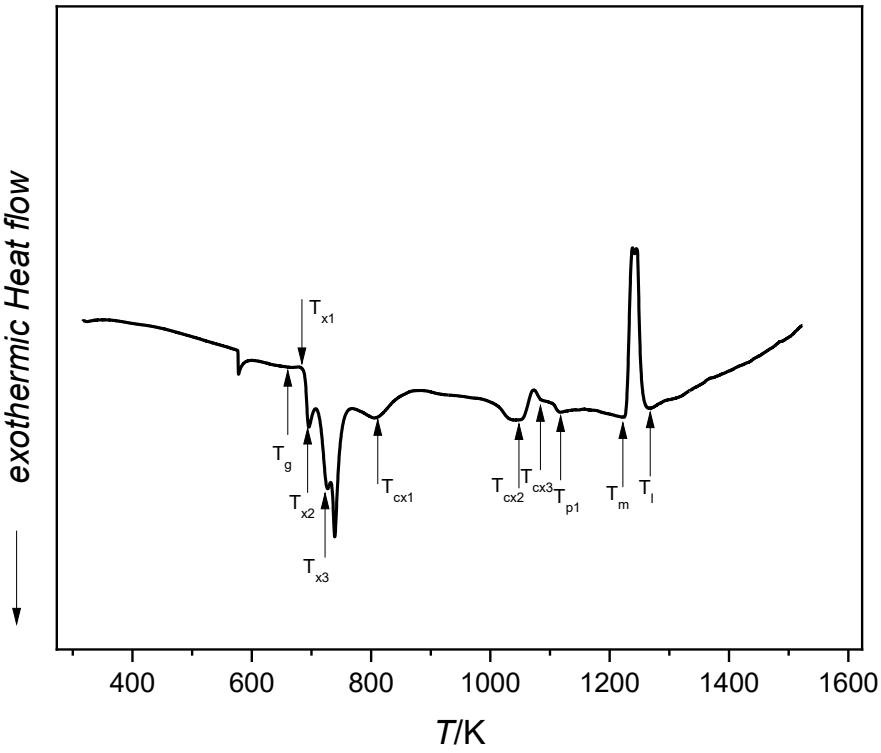

Figure 20: DSC curve of $Fe_{60}Co_{15}Ni_5P_{13}C_7$ at a 20 $Kmin^{-1}$ heating rate with marked points of the glass transition temperature T_g, crystallization temperatures T_x, Curie temperature T_c, phase transformation temperature T_p, melting temperature T_m, and liquidus temperature T_l.

Based on the high-temperature DSC curve, temperatures before and after each crystallization point were used for isothermal heat treatment for 60 seconds with a 20 $Kmin^{-1}$ heating and cooling rate. The heat treatments were conducted inside the DSC under a high purity argon atmosphere. The heat-treated samples were then analyzed by XRD.

Table 2: Summarized thermal properties of $Fe_{60}Co_{15}Ni_5P_{13}C_7$ measured by high-temperature DSC at 20 $Kmin^{-1}$

Alloy	**T_g ± 1 (K)**	**T_{x1} ± 1 (K)**	**T_{x2} ± 1 (K)**	**T_{x3} ± 1 (K)**	**T_{liq} ± 1 (K)**	**ΔT_x ± 2 (K)**	**T_{rg}**
$Fe_{60}Co_{15}Ni_5P_{13}C_7$	673	684	706	732	1249	11.4	0.54

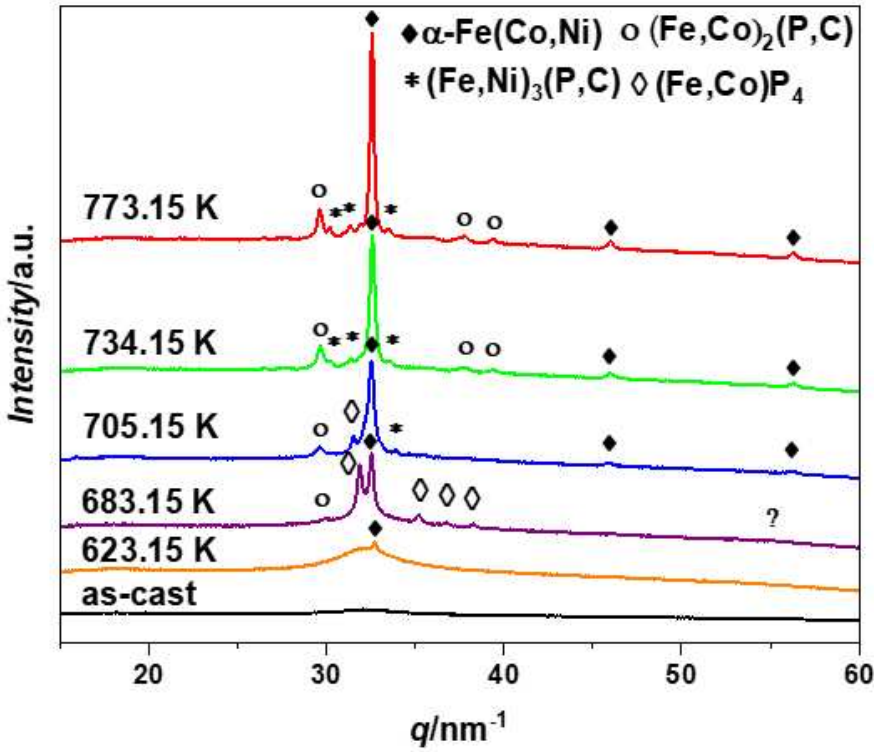

Figure 21: XRD curves of the $Fe_{60}Co_{15}Ni_5P_{13}C_7$ as-cast ribbon after several heat treatments.

The XRD analysis (Figure 21) shows no sharp peak for the as-cast ribbon, indicating amorphicity. At 623 ± 1 K, the first crystallization of α-Fe(Co, Ni) occurs. At 683 ± 1 K, a second prominent peak and a series of smaller peaks at higher q appeared, which disappeared after annealing at a higher temperature indicating a metastable phase. The metastable peaks between 30 and 40 nm^{-1} correspond to (Fe, Co)P_4. The peak at ~50 nm^{-1} has yet to be determined. These metastable phases are hard to detect as most databases are for phases in equilibrium. The metastable peaks disappear at 705 ± 1 K, and (Fe, Co)$_2$(P, C) and traces of (Fe, Ni)$_3$(P, C) start to crystalize. As the first crystallization depletes the amorph matrix from Fe, Ni, and Co atoms, and since the formation of (Fe, Co)$_2$(P, C) and (Fe, Ni)$_3$(P, C) requires high amounts of Fe atoms, their formation is slowed down.

Additionally, Flash differential scanning calorimetry experiments (Figure 22) at various high heating rates have been conducted. For this alloy, a new as-cast sample was measured for each curve. This was because the melting point of this alloy was slightly higher than the maximum temperature of the used machine setup. Thus, it was impossible to melt and cool the sample to amorphize it again. The measurements were conducted for heating rates between 200 – 13000 Ks^{-1}. The noise to signal ratio was insufficient for lower heating rates, and for higher heating rates,

the chip broke because of thermal stresses during the heating or cooling of the sample. All measurements exhibit a clear glass transition, slowly increasing with a higher heating rate. For the lowest heating rate, the inflection point of the glass transition was at 754 ± 1 K and raised with a higher heating rate to 780 ± 1 K. As the alloy does not fully melt within the machine's limitations, only the onset of the melting peak was measured. It stayed nearly the same for all heating rates at 1244 ± 10 K. In this alloy, three crystallization peaks were observed at low heating rates. At high heating rates, only one peak was observed. This is either due to the suppression of the crystallization, thermal inertia, or the sensitivity of the used setup.

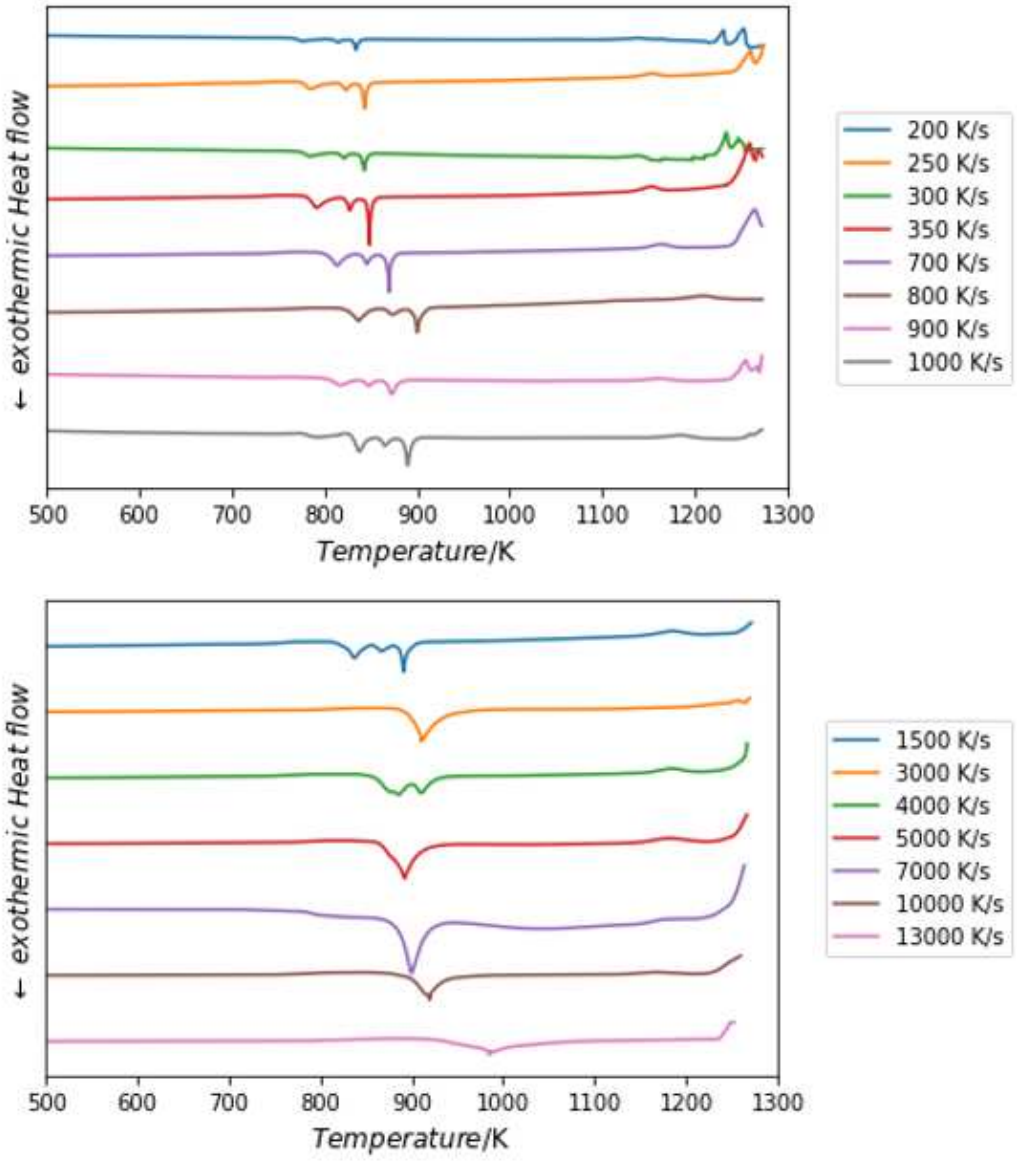

Figure 22: Flash DSC measurements of $Fe_{60}Co_{15}Ni_5P_{13}C_7$ at heating rates of 200 - 13000 Ks^{-1}.

The peaks at around 1173 ± 1 K indicate a phase transformation (α → γ) of iron. According to the ICTAC, the mass and heating rate product should not exceed 100 mg $Kmin^{-1}$. This means a maximum mass of 8333 ng for a heating rate of 200 Ks^{-1} and 128 ng for 13000 Ks^{-1}, respectively. Although the exact masses used in the Flash DSC measurements were not determined, the manufacturer suggests samples of around 5 ng and several micrograms. This leads to a higher probability of the influence of thermal inertia at higher heating rates.

Table 3: Summarized glass transition temperatures, the peak temperature of the first crystallization, and ΔT_x values of $Fe_{60}Co_{15}Ni_5P_{13}C_7$.

Heating rate (Ks^{-1})	**T_g ± 1 (K)**	**T_{x1} ± 1 (K)**	**ΔT_x ± 2 (K)**
200	754	776	21.5
300	752	784	31.9
350	756	791	35.4
700	745	813	68.0
800	767	837	69.2
900	749	817	67.9
1500	761	837	76.7
3000	808	911	103.0
4000	775	886	111.1
5000	782	893	110.3
7000	789	900	110.7
10000	780	919	139.0
13000	848	984	136.0

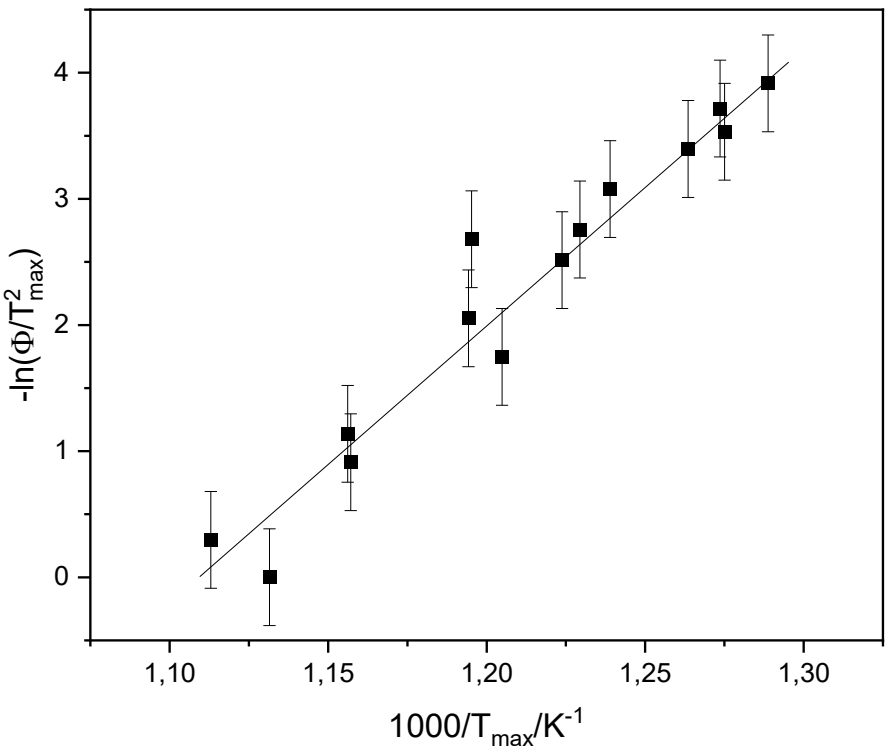

Figure 23: Kissinger plot for evaluating the first crystallization energy of $Fe_{60}Co_{15}Ni_5P_{13}C_7$ using the maximum temperatures of the peaks.

Analyzing the activation energy of the first crystallization peak (Figure 23) shows that all heating rates between 25 Ks^{-1} and 10000 Ks^{-1} are in good agreement with some deviations. This deviation can occur because of the different masses of the samples or different quality of the thermal contact during the measurement. According to the Kissinger method, this leads to an activation energy of 185.24 ± 0.46 $kJmol^{-1}$ calculated by the maximum temperature of the peaks. Analyzing the onset temperature of the peaks led to an activation energy of 146.65 ± 0.37 $kJmol^{-1}$. The lower activation energy analyzed by the onset temperatures indicates that nucleation is happening relatively easily, and the process is growth controlled. The final CHT diagram is shown in Figure 24.

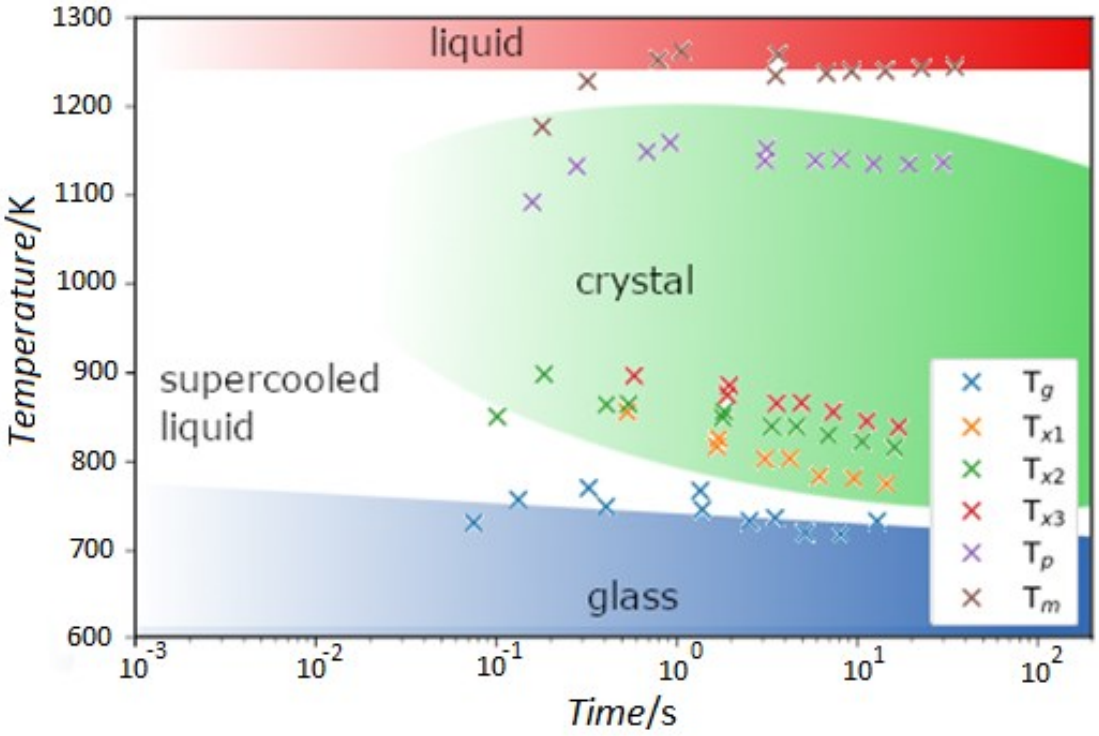

Figure 24: CHT Diagram of $Fe_{60}Co_{15}Ni_5P_{13}C_7$.

4.2. $Fe_{74}Mo_4Si_2P_{10}C_{7.5}B_{2.5}$

This alloy was cast with industrial-grade material by induction melting at 1373 K under a high purity argon atmosphere (99.9% pure). The high-temperature DSC curve of the as-cast rod is shown in Figure 25. The alloy exhibits a glass transition at 730 ± 1 K and three crystallization peaks at 762 ± 1 K, 811 ± 1 K, and 904 ± 1 K. After that, there is a small endothermic peak at 1020 ± 1 K that refers to Curie temperature, followed by an endothermic peak at around 1181 ± 1 K indicating an α→γ phase transformation of iron. The alloy starts to melt at 1208 ± 1 K. These temperatures were evaluated using the onset temperature of the corresponding peaks. The temperatures of the glass transition, the crystallization points, $\Delta T_{x,}$ and the reduced temperature, are summarized in Table 4.

Table 4: Summarized thermal properties of $Fe_{74}Mo_4Si_2P_{10}C_{7.5}B_{2.5}$ measured by high-temperature DSC at 20 $Kmin^{-1}$.

Alloy	**T_g ± 1 (K)**	**T_{x1} ± 1 (K)**	**T_{x2} ± 1 (K)**	**T_{x3} ± 1 (K)**	**T_{liq} ± 1 (K)**	**ΔT_x ± 2 (K)**	**T_{rg}**
$Fe_{74}Mo_4Si_2P_{10}C_{7.5}B_{2.5}$	730	762	811	904	1257	32.3	0.58

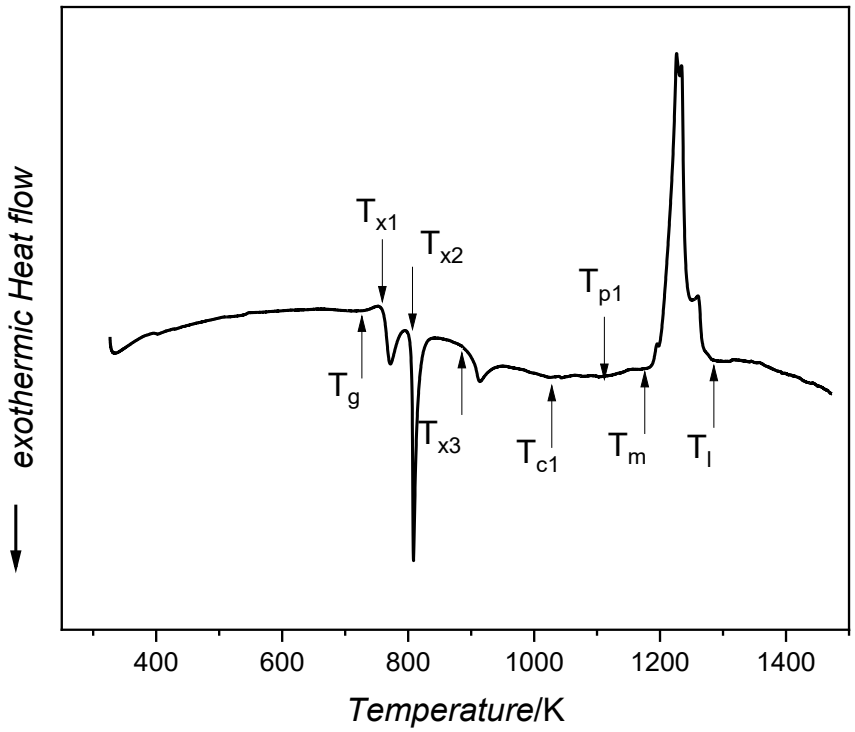

Figure 25: DSC measurement of $Fe_{74}Mo_4Si_2P_{10}C_{7.5}B_{2.5}$ at 20 $Kmin^{-1}$ with marked points of the glass transition temperature T_g, crystallization temperatures T_x, Curie temperature T_c, phase transformation temperature T_p, melting temperature T_m, and liquidus temperature T_l.

The XRD analysis (Figure 26:) shows no sharp peak and three broad amorph peaks for the as-cast ribbon, indicating amorphicity. At 778 ± 1 K, the first crystallization of $Fe_{23}(C, B)_6$ occurs, followed by the crystalization α-Fe, t-(Fe_3P), h-Fe_5Si_3, and c-FeSi at 823 ± 1 K.

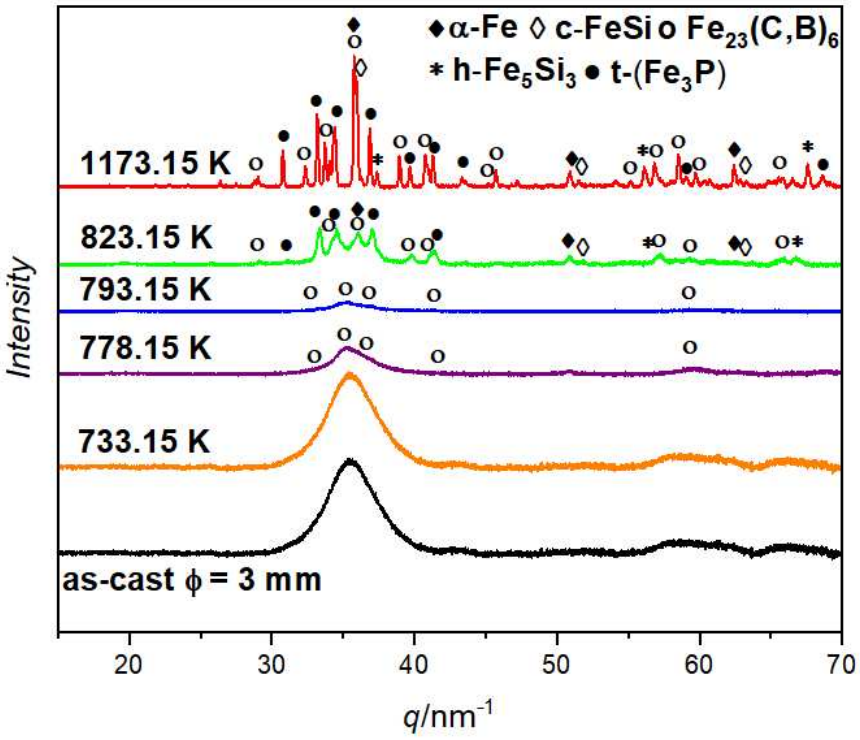

Figure 26: XRD measurements of the heat-treated $Fe_{74}Mo_4Si_2P_{10}C_{7.5}B_{2.5}$ samples.

The crystallization of the complex $Fe_{23}(C, B)_6$ structure is not expected, as more atomic ordering has to take place. It would be expected that more simple phases like α-Fe are the first to crystallize. Nanocrystals may already be present in the as-cast ribbon, acting as nucleation sites for the Borides. These nanocrystals could be so small that they are not visible in the XRD, and as they exhibit no thermodynamical phenomenon, they are also not visible in the DSC. This is also indicated by the very broad peaks in the as-cast rod. When nanocrystals become very small (less than 10 nm), the peaks become very broad, have low intensity, and often overlap with another [96].

Additionally, FDSC experiments at various high heating rates have been conducted. For this alloy, the sets from 25 – 1000 Ks^{-1} and 2000 – 10000 Ks^{-1} were each measured with one single sample. This was possible because the alloy's melting point measured on the DSC at 20 $Kmin^{-1}$ was well below the machine's maximum temperature. Measuring several heating rates with one sample would significantly reduce the effort of measuring CHT diagrams. Figure 27 shows a crystallization peak after each heating and cooling circle. Consequently, it can be said that the sample amorphized at least partly after each heating and cooling circle. All measurements exhibit a clear glass transition, slowly increasing with a higher heating rate. For the lowest heating rate, the inflection point of the glass transition was at 754 ± 1 K and raised to 780 ± 1 K at the highest heating rate.

The crystallization temperatures rise with higher heating rates, broadening the super-cooled liquid region ($\Delta T_x = T_x - T_g$). At high heating rates, only one peak was observed. Although the melting temperature stayed nearly the same, the liquidus temperature raises with higher heating rates well above the machine's maximum temperature of 1273 K (Figure 28). This indicates that the overheating between each run may not be sufficient to fully dissolute all heterogeneities. Mukherjee et al. [97] studied the effect of overheating in Zr-based BMGs. They observed an increase in the crystallization time when a certain overheating threshold is exceeded. This may be due to the dissolution of heterogeneities acting as nucleation sites.

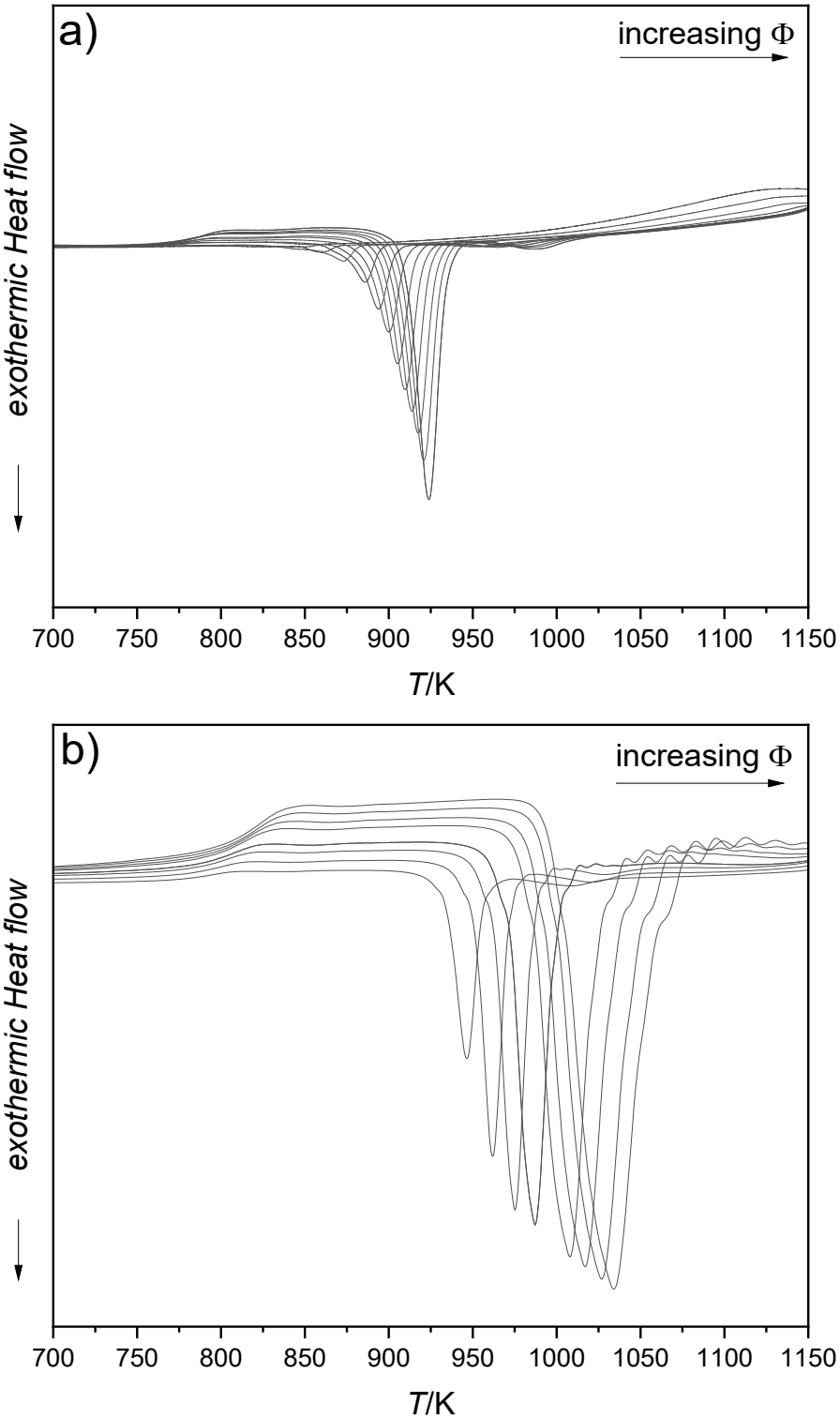

Figure 27: Overview of the crystallization peaks of $Fe_{74}Mo_4Si_2P_{10}C_{7.5}B_{2.5}$ for heating rates Φ between a) 25 - 1000 Ks^{-1} and b) 2000 – 10000 Ks^{-1}.

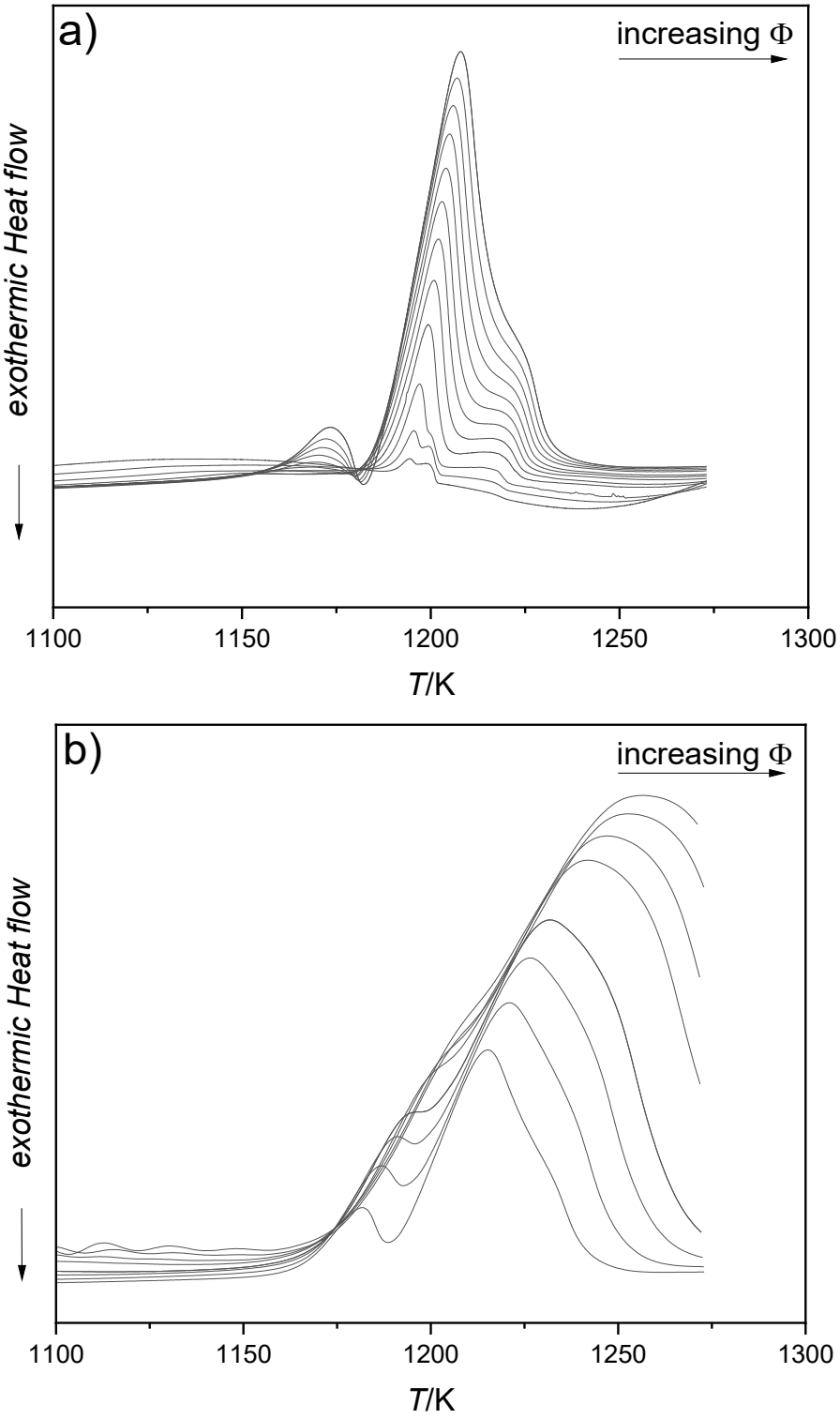

Figure 28: Overview of the melting peaks of $Fe_{74}Mo_4Si_2P_{10}C_{7.5}B_{2.5}$ for heating rates Φ between a) 25 - 1000 Ks^{-1} and b) 2000 – 10000 Ks^{-1}.

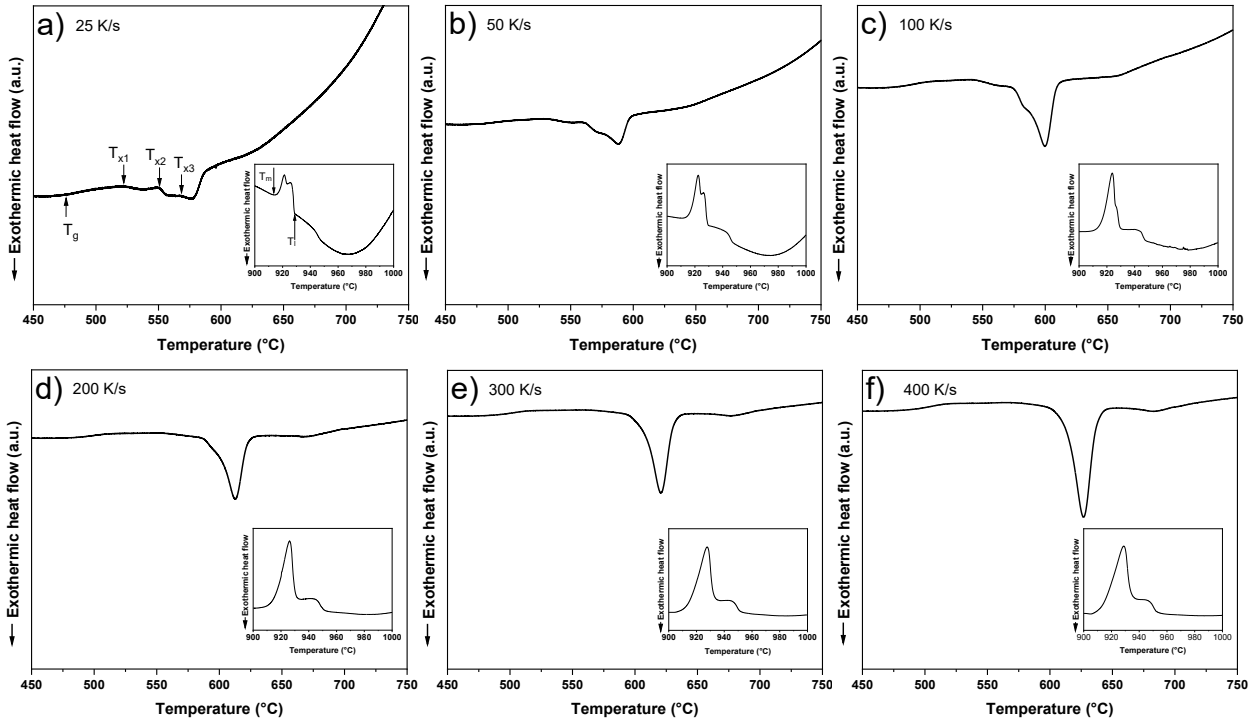

Figure 29: Flash DSC curves of $Fe_{74}Mo_4Si_2P_{10}C_{7.5}B_{2.5}$ for heating rates between a) 25 Ks^{-1} and l) 400 Ks^{-1} with insets of the melting peak.

Figure 29 shows the crystallization peak in detail. It can be seen that at heating rates between 25 Ks^{-1} and 100 Ks^{-1}, three overlapping crystallization peaks are observed. At higher heating rates, these three peaks become one single peak. This means that either the crystallization of the other two phases is suppressed or at least one phase is not fully dissolved at higher heating rates, as the melting threshold is not reached within the limitations of the machine.

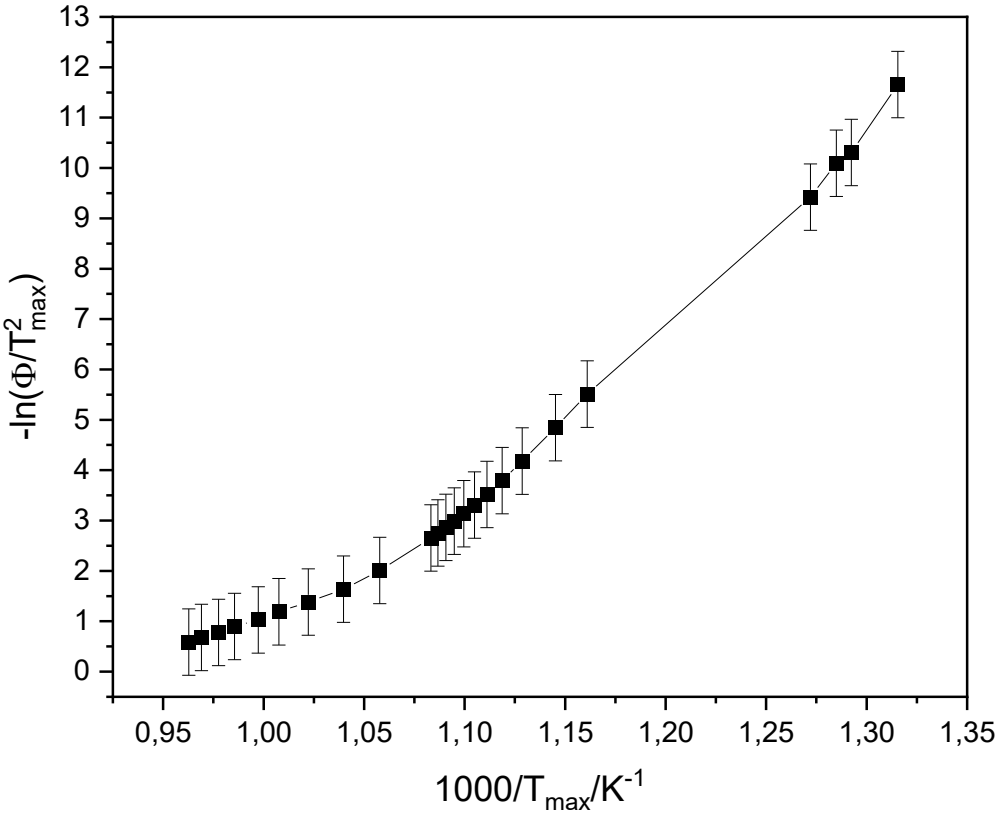

Figure 30: Kissinger plot for evaluating the first crystallization energy of Fe74Mo4Si2P10C7.5B2.5 using the maximum temperatures of the peaks.

DSC measurements at 5, 20, 25, and 50 $Kmin^{-1}$ have been conducted, leading to an activation energy of 425.05 ± 1.1 $kJmol^{-1}$ for the peak temperatures and 539.74 ± 1.4 $kJmol^{-1}$ for the onset temperatures. The higher activation energy derived from the onset temperatures indicates a nucleation-controlled process. Analyzing the activation energy of the maximum of the first crystallization peak shows that for the FDSC, relatively heating rates between 25 Ks^{-1} and 1000 $Ks^{-1,}$ the Kissinger method leads to an activation energy of 314.11 ± 0.72 $kJmol^{-1}$. Calculating the activation energy with the onset temperatures leads to 196.25 ± 0.48 $kJmol^{-1}$. The activation energy of the onset corresponds to the nucleation energy, whereas the energy derived from the maximum temperature corresponds to the energy for the crystallite growth. The main difference between the DSC and FDSC measurements are the heating rates, the mass of the samples, and the use of one sample for each set of heating rates between 25 - 1000 $Kmin^{-1}$ and 2000 – 10000 $Kmin^{-1}$. There is a significant reduction of 135% in activation energy for crystal growth between the low and medium heating rates. Also, the activation energy of the nucleation is reduced by 275% and is even lower than the activation energy for growth at medium heating rates. This indicates significant amounts of nuclei in the sample, so the growth of the nuclei controls the process. At higher heating rates, the slope becomes curved. This is an effect caused by the high

heating rates. The high heating rates cause the crystallization to occur at higher temperatures, ultimately approaching T_m. This decreases the free energy driving force for crystallization ΔG, and the growth rate U tends to zero [53]. This curvature is a sign of a fragile liquid.

Angell [45] classifies “strong” liquids as network-forming liquids that show an Arrhenius or near-Argenius temperature-dependence of η. A “fragile” liquid shows high η just above T_g, decreasing with rising temperature. The curvature may also be due to thermal inertia, which becomes more relevant at higher heating rates. Also, the change between these two slopes was exactly when a new sample was used. It is possible that the used sample was already partly crystallized. This can happen when two parts of the ribbon come in contact right after the melt spinning process, leading to a hotspot that cools slower than the rest of the ribbon. Another explanation is that the overheating of the sample is not high enough to dissolve all nanocrystals in the sample fully. Figure 31 shows the CHT diagram for heating rates between 25 – 10000 Ks^{-1}. In Table 5, the thermal properties T_g, T_{x1}, T_l, T_{rg}, and ΔT_x are summarized.

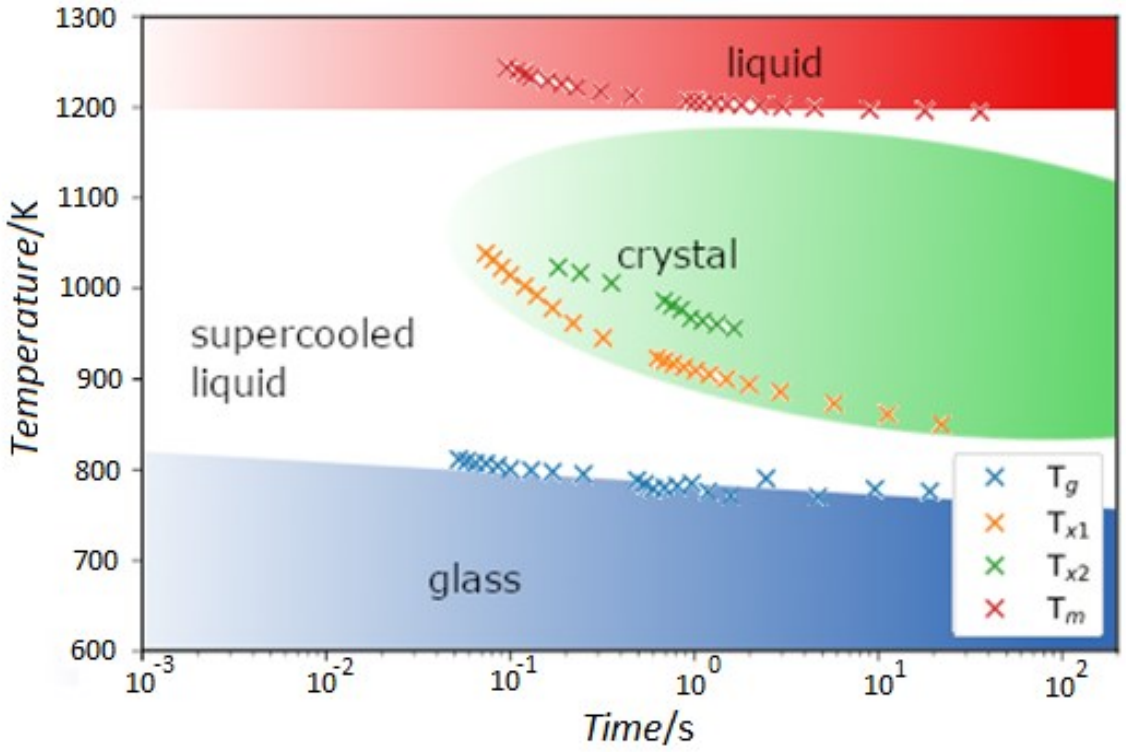

Figure 31: CHT Diagram of $Fe_{74}Mo_4Si_2P_{10}C_{7.5}B_{2.5}$.

Table 5: Summarized glass transition temperatures, peak temperatures of the first crystallization, and ΔT_x values of $Fe_{74}Mo_4Si_2P_{10}C_{7.5}B_{2.5}$.

Heating rate (Ks^{-1})	**T_g ± 1 (K)**	**T_{x1} ± 1 (K)**	**T_l ± 1 (K)**	**ΔT_x ± 2 (K)**	**T_{rg}**
25	776	850	1221	73,9	0.64
50	779	861	1221	82,6	0.64
100	770	873	1221	103,5	0.63
200	790	886	1224	95,6	0.65
300	771	894	1224	122,6	0.63
400	776	900	1226	124,3	0.63
500	785	905	1226	120,3	0.64
600	782	909	1227	127,3	0.64
700	780	913	1229	133,4	0.63
800	779	917	1229	137,8	0.63
900	784	920	1230	135,9	0.64
1000	788	923	1231	134,7	0.64
2000	795	945	1242	150,2	0.64
3000	797	962	1250	164,3	0.64
4000	799	978		178,9	
5000	801	992		191,9	
6000	804	1006		198,3	
7000	807	1017		208,0	
8000	807	1023		215,7	
9000	810	1032		222,3	
10000	812	1039		227,1	

In-situ SXRD measurements during Flash DSC were conducted at the Petra III Synchrotron (DESY Hamburg). A Pilatus 3 2M detector from Dectris (Swiss) was used. The CdTe sensor is capable of detecting 250 frames per second. The 2D data was evaluated by a self-written script attached in the appendix. Figure 32 shows the structural evolution during a fast heating rate of 250 Ks^{-1}. Compared with the DSC curve in Figure 33, it can be seen that the process happens in

three defined steps. The first crystallization peak starts at 866 ± 1 K and is relatively broad. As stated before, the first peak corresponds to the formation of $Fe_{23}(C, B)_6$, a complex structure that needs a lot of reorganization of the atoms. The second peak at 905 ± 1 K is much sharper and corresponds to the crystallization of α-Fe, indicating spontaneous nucleation and grain growth with much less atomic rearrangement. The third peak at 1011 ± 1 K corresponds to the crystallization of t-(Fe_3P) and c-FeSi. It can also be observed that a peak that was formed in the third crystallization vanishes at the isothermal hold at 1223 ± 1 K. It can be seen that no additional XRD are forming during each crystallization period. Therefore, it can be stated that these crystallization events are one-step processes.

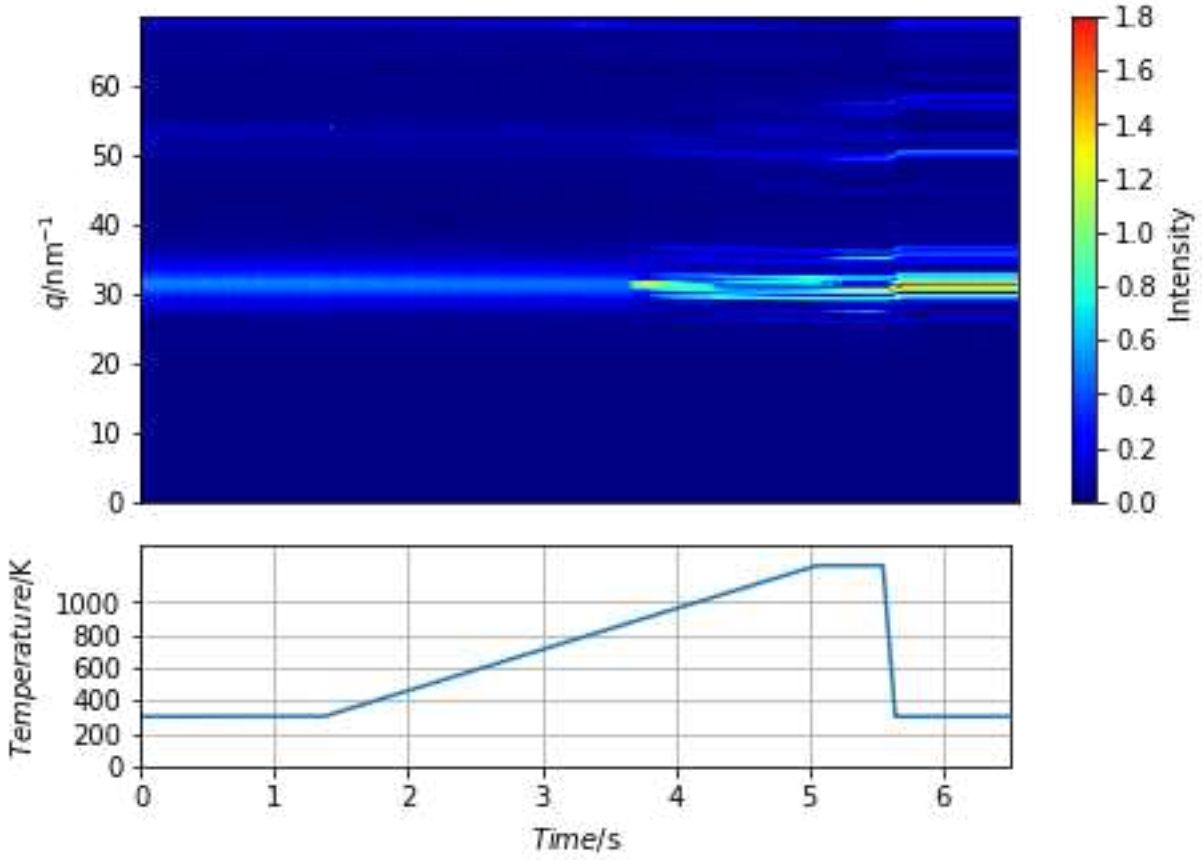

Figure 32: Intensity map and temperature curve of the SXRD measurement of $Fe_{74}Mo_4Si_2P_{10}C_{7.5}B_{2.5}$.

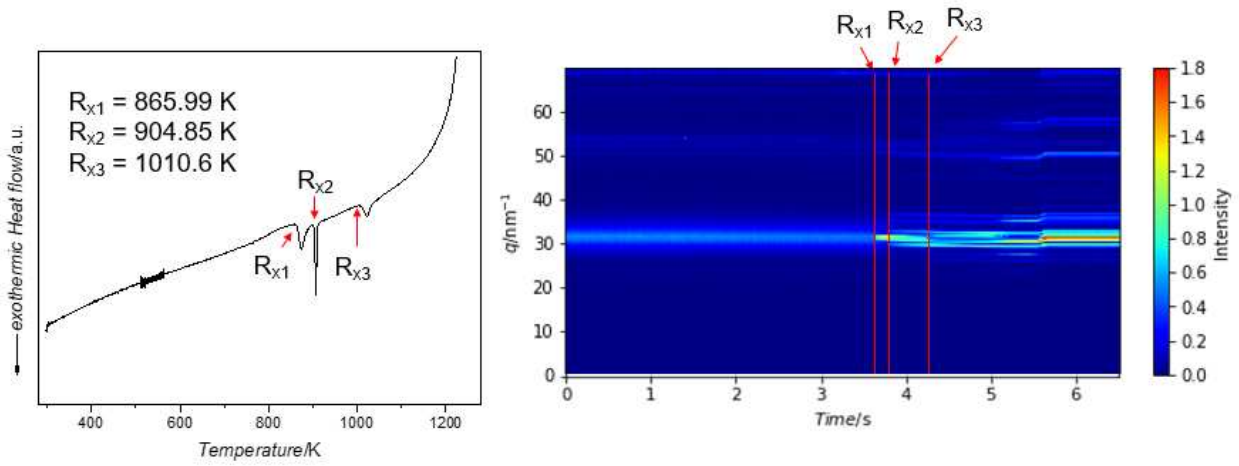

Figure 33: Comparison between the in-situ Flash DSC and XRD data at 200 Ks^{-1}.

5. Summary

- Analyzing ΔT_x, T_{rg}, and the size of the supercooled liquid region, $Fe_{74}Mo_4Si_2P_{10}C_{7.5}B_{2.5}$ exhibits a significantly higher glass-forming ability than $Fe_{60}Co_{15}Ni_5P_{13}C_7$. The higher glass-forming ability is a consequence of the higher number of constituent elements of $Fe_{74}Mo_4Si_2P_{10}C_{7.5}B_{2.5}$ and the high impact of carbon, boron, and silicon on the glass-forming ability.

- Fast DSC measurements with high heating rates were successfully conducted at $Fe_{60}Co_{15}Ni_5P_{13}C_7$. The alloy exhibits three crystallization events that are observable even at relatively high heating rates of 4000 Ks^{-1}.

- The melting threshold of $Fe_{74}Mo_4Si_2P_{10}C_{7.5}B_{2.5}$ cannot be reached within the FDSC's limitations, resulting in considerable amounts of nano-crystalline material, hindering diffusion upon annealing. Also, the matrix gets enriched on B by the formation of $Fe_{23}B_6$, resulting in a higher glass-forming ability and only one crystallization peak at higher heating rates.

- In $Fe_{60}Co_{15}Ni_5P_{13}C_7$ alloy, the α-iron phase is the first to crystallize, which can be used to improve magnetic properties. In the $Fe_{74}Mo_4Si_2P_{10}C_{7.5}B_{2.5,}$ the first phase to crystalize was the $Fe_{23}B_6$ phase which is good for the glass-forming ability but usually degrades the magnetic properties.

- A python-script for the preparation and evaluation of synchrotron data was developed. Multiprocessing was implemented, reducing the integration time by ~40 times. The script also offers an easy way of removing the background as well as the peaks of the measurement chip.

- The synchrotron measurements on $Fe_{74}Mo_4Si_2P_{10}C_{7.5}B_{2.5}$ clearly show that at 250 Ks^{-1}, three individual crystallization events can be observed. However, in the laboratory FDSC measurements, only one peak was observable, indicating crystallization and no sufficient overheating in the first normalization run. More complex phases such as $Fe_{23}B_6$ need a higher melting threshold than simple crystalline phases like α-Fe. Because of this, it is assumed that $Fe_{23}B_6$ may be the residual phase.

6. Conclusion and Outlook

In this work, the thermal and structural properties of two alloys, $Fe_{60}Co_{15}Ni_5P_{13}C_7$ and $Fe_{74}Mo_4Si_2P_{10}C_{7.5}B_{2.5,}$ have been studied. They were produced as ribbons and rods and have been analyzed by XRD and DSC. Isothermal annealing at various temperatures and subsequent XRD measurements have been conducted to determine the crystallized phases. Additionally, FDSC measurements were performed to investigate the crystallization behavior at high heating rates. In order to investigate the time and temperature evolution of crystallization during high heating rates, $Fe_{74}Mo_4Si_2P_{10}C_{7.5}B_{2.5}$ was investigated by in-situ Flash DSC during synchrotron XRD.

- Heat treatments have been successfully applied. In $Fe_{60}Co_{15}Ni_5P_{13}C_7$ alloy, the α-Iron phase is the first to crystallize, which can be used to improve magnetic properties. In the $Fe_{74}Mo_4Si_2P_{10}C_{7.5}B_{2.5,}$ the first phase to crystalize was the $Fe_{23}B_6$ phase which is good for the glass-forming ability but usually decreases the magnetic properties. In order to determine and control the size and distribution of the nanocrystals, a detailed study of the dependence on time and temperature needs to be conducted.

- The composition and size of the nanocrystals can be investigated by transmission electron microscopy (TEM) or atom probe tomography.

- FDSC has proven to be a reliable tool to investigate the glass-forming ability of iron-based BMGs as long as the liquidus temperature does not exceed the machine's maximum temperature and a sufficient melting threshold is ensured.

- An often stated drawback of the Kissinger method is the assumption of a single-step process for determining the activation energy of the first crystallization. In-situ flash DSC during high-energy synchrotron XRD offers the possibility of investigating the time evolution of the crystallization. By directly comparing FDSC and XRD data, it is easily observable if the crystallization is a one or multi-step process.

Table 6: Summary of the thermal properties of the investigated samples at a 20 Kmin^{-1}heating rate.

Alloy	**T_g ± 1 (K)**	**T_{x1} ± 1 (K)**	**T_{x2} ± 1 (K)**	**T_{x3} ± 1 (K)**	**T_{liq} ± 1 (K)**	**ΔT_x ± 2 (K)**	**T_{rg}**
$Fe_{60}Co_{15}Ni_5P_{13}C_7$	673	684	706	732	1249	11.4	0.54
$Fe_{74}Mo_4Si_2P_{10}C_{7.5}B_{2.5}$	730	762	811	904	1257	32.3	0.58

7. References

1. Ramanan, V. R. & Carlen, M. 40 ABB review 2|12 ABB's amorphous metal distribution transformers are maximizing energy savings.
2. Azuma, D. & Hasegawa, R. Audible noise from amorphous metal and silicon steel-based transformer core. *IEEE Trans. Magn.* **44**, 4104–4106 (2008).
3. Makino, A., Kubota, T., Chang, C., Makabe, M. & Inoue, A. FeSiBP bulk metallic glasses with high magnetization and excellent magnetic softness. *J. Magn. Magn. Mater.* **320**, 2499–2503 (2008).
4. Stoica, M. Fe-Based Bulk Metallic Glasses. (2017) doi:10.1007/978-3-658-17018-9.
5. Nicoara, M. *et al.* Low Young's modulus Ti-based porous bulk glassy alloy without cytotoxic elements. *Acta Biomater.* **36**, 323–331 (2016).
6. Suryanarayana, C. & Inoue, A. *Bulk metallic glasses: Second edition*. *Bulk Metallic Glasses: Second Edition* (CRC Press, 2017). doi:10.1201/9781315153483.
7. Mahbooba, Z. *et al.* Additive manufacturing of an iron-based bulk metallic glass larger than the critical casting thickness. *Appl. Mater. Today* **11**, 264–269 (2018).
8. Gu, X. J., Poon, S. J. & Shiflet, G. J. Mechanical properties of iron-based bulk metallic glasses. *J. Mater. Res.* **22**, 344–351 (2007).
9. Yang, W. *et al.* Oxygen-driven impurities scavenging before solidification of Fe-based metallic glasses. *J. Alloys Compd.* **773**, 401–412 (2019).
10. Ramasamy, P., Stoica, M., Calin, M. & Eckert, J. Effect of Cu and Gd on structural and magnetic properties of Fe-Co-B-Si-Nb metallic glasses. *Solid State Phenom.* **254**, 60–64 (2016).
11. Ramasamy, P. Soft Ferromagnetic Bulk Metallic Glasses with Enhanced Mechanical Properties. 159 (2017).
12. Patel, S. K., Swain, B. K., Behera, A. & Mohapatra, S. S. Metallic Glasses: A Revolution in Material Science. *Met. Glas.* (2020) doi:10.5772/INTECHOPEN.90165.
13. Klement, W., Willens, R. H. & Duwez, P. Non-crystalline structure in solidified Gold-Silicon alloys. *Nature* **187**, 869–870 (1960).
14. DAVIES, H. A., AUCOTE, J. & HULL, J. B. Amorphous Nickel produced by Splat Quenching. *Nat. Phys. Sci. 1973 246149* **246**, 13–14 (1973).
15. Budhani, R. C., Goel, T. C. & Chopra, K. L. Melt-spinning technique for preparation of metallic glasses. *Bull. Mater. Sci. 1982 45* **4**, 549–561 (1982).
16. Lavernia, E. J. & Srivatsan, T. S. The rapid solidification processing of materials: science, principles, technology, advances, and applications. *J. Mater. Sci. 2009 452* **45**, 287–325 (2010).
17. Sharma, J., Suresh, K. G., Raja, M. M. & Walke, P. Martensitic Transition, Magnetic, Microstructural and Exchange Bias Properties of Melt Spun Ribbons of Mn-Ni-Sn Shape Memory Heusler Alloy. *Front. Pharmacol.* **11**, 343 (2020).
18. Lashgari, H. R., Ferry, M. & Li, S. Additive manufacturing of bulk metallic glasses: Fundamental principle, current/future developments and applications. *Journal of Materials Science and Technology* vol. 119 131–149 (2022).
19. Pauly, S., Wang, P., Kühn, U. & Kosiba, K. Experimental determination of cooling rates in

selectively laser-melted eutectic Al-33Cu. *Addit. Manuf.* **22**, 753–757 (2018).

20. Best, J. P. *et al.* Relating fracture toughness to micro-pillar compression response for a laser powder bed additive manufactured bulk metallic glass. *Mater. Sci. Eng. A* **770**, 138535 (2020).
21. Pauly, S. *et al.* Processing metallic glasses by selective laser melting. *Mater. Today* **16**, 37–41 (2013).
22. Zhang, P., Tan, J., Tian, Y., Yan, H. & Yu, Z. Research progress on selective laser melting (SLM) of bulk metallic glasses (BMGs): a review. *Int. J. Adv. Manuf. Technol. 2021 1187* **118**, 2017–2057 (2021).
23. Chen, C., Shen, Y. & Tsai, H. L. A foil-based additive manufacturing technology for metal parts. *J. Manuf. Sci. Eng. Trans. ASME* **139**, (2017).
24. Yang, D. *et al.* Atomic-level understanding of weakening crystallization in additive manufactured ternary Fe-based metallic glasses with Ni addition. *J. Non. Cryst. Solids* **582**, 121435 (2022).
25. Li, X. P., Kang, C. W., Huang, H. & Sercombe, T. B. The role of a low-energy–density re-scan in fabricating crack-free Al85Ni5Y6Co2Fe2 bulk metallic glass composites via selective laser melting. *Mater. Des.* **63**, 407–411 (2014).
26. Chen, H. S. Glassy metals. *Reports Prog. Phys.* **43**, 353 (1980).
27. Suryanarayana, C. & Inoue, A. Iron-based bulk metallic glasses. *Int. Mater. Rev.* **58**, 131–166 (2013).
28. Onorato, P. I. K. & Uhlmann, D. R. Nucleating heterogeneities and glass formation. *J. Non. Cryst. Solids* **22**, 367–378 (1976).
29. Barandiarán, J. M. & Colmenero, J. Continuous cooling approximation for the formation of a glass. *J. Non. Cryst. Solids* **46**, 277–287 (1981).
30. Lu, Z. P. & Liu, C. T. Role of minor alloying additions in formation of bulk metallic glasses: A review. *J. Mater. Sci.* **39**, 3965–3974 (2004).
31. Gao, J. E. *et al.* Fe-based bulk metallic glass composites without any metalloid elements. *AcMat* **61**, 3214–3223 (2013).
32. Wu, Y. *et al.* Effects of metalloid elements on the glass-forming ability of Fe-based alloys. *J. Alloys Compd.* **467**, 187–190 (2009).
33. Schroers, J. Bulk Metallic Glasses. *Phys. Today* **66**, 32 (2013).
34. Shen, J., Chen, Q., Sun, J., Fan, H. & Wang, G. Exceptionally high glass-forming ability of an FeCoCrMoCBY alloy. *Appl. Phys. Lett.* **86**, 151907 (2005).
35. Turnbull, D. Under What Conditions Can A Glass Be Formed? *Contemp. Phys.* **10**, 473–488 (1969).
36. Peker, A. & Johnson, W. L. A highly processable metallic glass: Zr41.2Ti13.8Cu12.5Ni10.0Be22.5. *Appl. Phys. Lett.* **63**, 2342 (1998).
37. Egami, T. & Waseda, Y. Atomic size effect on the formability of metallic glasses. *J. Non. Cryst. Solids* **64**, 113–134 (1984).
38. Inoue, A. Recent Progress of Zr-Based Bulk Amorphous Alloys. *Sci. Reports Rerearch Institutes Tohoku Univ. Ser. A-Physics* **42**, (1996).
39. Inoue, A. *Bulk amorphous alloys: preparation and fundamental characteristics*. *Materials*

Science Foundation (Trans Tech, 1998).

40. INOUE, A. Stabilization of Supercooled Liquid and Opening-up of Bulk Glassy Alloys. *Proc. Japan Acad. Ser. B* **73**, 19–24 (1997).
41. Li, M. X. *et al.* Data-driven discovery of a universal indicator for metallic glass forming ability. *Nat. Mater.* **21**, 165–172 (2022).
42. Greer, A. L. & Ma, E. Bulk Metallic Glasses: At the Cutting Edge of Metals Research. *MRS Bull.* **32**, 611–619 (2007).
43. Inoue, A. Stabilization of metallic supercooled liquid and bulk amorphous alloys. *Acta Mater.* **48**, 279–306 (2000).
44. Wang, W. H., Dong, C. & Shek, C. H. Bulk metallic glasses. *Mater. Sci. Eng. R Reports* **44**, 45–89 (2004).
45. Angell, C. A. Formation of Glasses from Liquids and Biopolymers. *New Ser.* **267**, 1924–1935 (1995).
46. Zhang, N., Byrne, C. J., Browne, D. J. & Gilchrist, M. D. Towards nano-injection molding. *Mater. Today* **15**, 216–221 (2012).
47. Kui, H. W. & Turnbull, D. Melting of Ni40Pd40P20 glass. *Appl. Phys. Lett.* **47**, 796 (1998).
48. Schroers, J., Johnson, W. L. & Busch, R. Crystallization kinetics of the bulk-glass-forming Pd43Ni10Cu27P20 melt. *Appl. Phys. Lett.* **77**, 1158 (2000).
49. Bartsch, A., Rätzke, K., Meyer, A. & Faupel, F. Dynamic arrest in multicomponent glass-forming alloys. *Phys. Rev. Lett.* **104**, 195901 (2010).
50. Yu, H. B., Samwer, K., Wu, Y. & Wang, W. H. Correlation between β relaxation and self-diffusion of the smallest constituting atoms in metallic glasses. *Phys. Rev. Lett.* **109**, 095508 (2012).
51. Aljerf, M., Georgarakis, K. & Yavari, A. R. Shaping of metallic glasses by stress-annealing without thermal embrittlement. *Acta Mater.* **59**, 3817–3824 (2011).
52. Wang, A. *et al.* Fe-based amorphous alloys for wide ribbon production with high Bs and outstanding amorphous forming ability. *J. Alloys Compd.* **630**, 209–213 (2015).
53. Orava, J. & Greer, A. L. Kissinger method applied to the crystallization of glass-forming liquids: Regimes revealed by ultra-fast-heating calorimetry. *Thermochim. Acta* **603**, 63–68 (2015).
54. Köster, U. & Herold, U. Crystallization of metallic glasses. in 225–259 (Springer, Berlin, Heidelberg, 1981). doi:10.1007/3540104402_10.
55. Vyazovkin, S. Kissinger Method in Kinetics of Materials: Things to Beware and Be Aware of. *Molecules* **25**, 2813 (2020).
56. Vyazovkin, S. *et al.* ICTAC Kinetics Committee recommendations for analysis of multi-step kinetics. *Thermochimica Acta* vol. 689 178597 (2020).
57. Borchardt, H. J. & Daniels, F. The Application of Differential Thermal Analysis to the Study of Reaction Kinetics. *J. Am. Chem. Soc.* **79**, 41–46 (1957).
58. Vyazovkin, S. *et al.* ICTAC Kinetics Committee recommendations for collecting experimental thermal analysis data for kinetic computations. *Thermochim. Acta* **590**, 1–23 (2014).
59. Greer, A. L. Metallic Glasses. *Science (80-.).* **267**, 1947–1953 (1995).

60. Masumoto, T. & Suzuki, K. *Proceedings of the Fourth International Conference on Rapidly Quenched Metals: Sendai, Japan, August 24-28, 1981*. vol. 2 (Japan Institute of metals, 1982).

61. Ok, H. N. & Morrish, A. H. Origin of the perpendicular anisotropy in amorphous Fe82B12Si6 ribbons. *Phys. Rev. B* **23**, 2257–2261 (1981).

62. Croat, J. J., Herbst, J. F., Lee, R. W. & Pinkerton, F. E. Pr-Fe and Nd-Fe-based materials: A new class of high-performance permanent magnets (invited). *J. Appl. Phys.* **55**, 2078 (1998).

63. H. G. Hillenbrand, E. Hornbogen, U. K. No Title. *Pro- ceedings Fourth Int. Conf. Rapidly Quenched Met. T. Masumoto K. Suzuki* 1369–1372 (1982).

64. Kim, Y. H., Inoue, A. & Masumoto, T. Ultrahigh Tensile Strengths of Al88Y2Ni9M1 (M=Mn or Fe) Amorphous Alloys Containing Finely Dispersed fcc-Al Particles. *Mater. Trans. JIM* **31**, 747–749 (1990).

65. Chen, H., He, Y., Shiflet, G. J. & Poon, S. J. Scripta Metallurg. *Mater* **25**, 1421 (1991).

66. K. Higashi, E. al. Superplastic behavior in a mechanically alloyed aluminum composite reinforced with SiC particulates. *Scr. Met. Mater.* **26**, (1992).

67. Fornell, J. *et al.* Enhanced mechanical properties due to structural changes induced by devitrification in Fe–Co–B–Si–Nb bulk metallic glass. *Acta Mater.* **58**, 6256–6266 (2010).

68. Freed, R. L. & Vander Sande, J. B. The metallic glass Cu56Zr44: Devitrification and the effects of devitrification on mechanical properties. *Acta Metall.* **28**, 103–121 (1980).

69. Yoshizawa, Y., Oguma, S. & Yamauchi, K. New Fe-based soft magnetic alloys composed of ultrafine grain structure. *J. Appl. Phys.* **64**, 6044–6046 (1988).

70. Suzuki, K., Makino, A., Inoue, A. & Masumoto, T. Soft magnetic properties of nanocrystalline bcc Fe-Zr-B and Fe-M-B-Cu (M=transition metal) alloys with high saturation magnetization (invited). *J. Appl. Phys.* **70**, 6232 (1998).

71. Tong, X. *et al.* Structural origin of magnetic softening in a Fe-based amorphous alloy upon annealing. *J. Mater. Sci. Technol.* **96**, 233–240 (2022).

72. A. Datta, N. J. De Cristofaro, L. A. D. Pro- ceedings of the Fourth International Conference on Rapidly Quenched Metals. *T. Masumoto K. Suzuki* 1007–1010 (1982).

73. W. L. Johnson. Superconductivity in metallic glasses. *Glas. Met. I, H. J. Güntherodt H. Beck, Eds.* 191–223 (1981) doi:10.1007/3540104402_9.

74. Zhang, Y., Wang, Y. & Makino, A. Structural and magnetic properties on the Fe-B-P-Cu-W nano-crystalline alloy system. *AIP Adv.* **8**, 047703 (2017).

75. Jiang, L., Zhang, Y., Tong, X., Suzuki, T. & Makino, A. Unique influence of heating rate on the magnetic softness of Fe81.5Si0.5B4.5P11Cu0.5C2 nanocrystalline alloy. *J. Magn. Magn. Mater.* **471**, 148–152 (2019).

76. Inoue, A., Shen, B. L., Koshiba, H., Kato, H. & Yavari, A. R. Ultra-high strength above 5000 MPa and soft magnetic properties of Co–Fe–Ta–B bulk glassy alloys. *Acta Mater.* **52**, 1631–1637 (2004).

77. Stoica, M. *et al.* Structure evolution of soft magnetic (Fe36Co36B19.2Si4.8Nb4)100-xCux (x = 0 and 0.5) bulk glassy alloys. *Acta Mater.* **95**, 335–342 (2015).

78. Tiberto, P., Baricco, M., Olivetti, E. & Piccin, R. Magnetic Properties of Bulk Metallic Glasses. *Adv. Eng. Mater.* **9**, 468–474 (2007).

79. Herzer, G. Grain Size Dependence of Coercivity and Permeability in Nanocrystalline Ferromagnets. *IEEE Trans. Magn.* **26**, 1397–1402 (1990).

80. Yoshizawa, Y., Oguma, S. & Yamauchi, K. New Fe-based soft magnetic alloys composed of ultrafine grain structure. *J. Appl. Phys.* **64**, 6044 (1998).

81. Suzuki, K., Makino, A., Inoue, A. & Masumoto, T. Low core losses of nanocrystalline Fe–M–B (M=Zr, Hf, or Nb) alloys. *J. Appl. Phys.* **74**, 3316 (1998).

82. Willard, M. A. *et al.* Magnetic properties of HITPERM (Fe,Co)88Zr7B4Cu1 magnets. *J. Appl. Phys.* **85**, 4421 (1999).

83. Ramasamy, P. Soft Ferromagnetic Bulk Metallic Glasses with Enhanced Mechanical Properties (Dissertation). 159 (2017).

84. Danley, R. L. New heat flux DSC measurement technique. *Thermochim. Acta* **395**, 201–208 (2002).

85. Haines, P. J., Reading, M. & Wilburn, F. W. Differential Thermal Analysis and Differential Scanning Calorimetry. *Handb. Therm. Anal. Calorim.* **1**, 279–361 (1998).

86. Toledo, M. Thermal Analysis Excellence Flash DSC 2+ Manual.

87. Mobilio, S., Boscherini, F. & Meneghini, C. Synchrotron radiation: Basics, methods and applications. *Synchrotron Radiat. Basics, Methods Appl.* 1–799 (2015) doi:10.1007/978-3-642-55315-8.

88. Van Rossum, G. & Drake, F. L. *Python 3 Reference Manual*. (CreateSpace, 2009).

89. Ashiotis, G. *et al.* The fast azimuthal integration Python library: pyFAI. *urn:issn:1600-5767* **48**, 510–519 (2015).

90. Knudsen, E. B., Sørensen, H. O., Wright, J. P., Goret, G. & Kieffer, J. FabIO: Easy access to two-dimensional X-ray detector images in Python. *J. Appl. Crystallogr.* **46**, 537–539 (2013).

91. de Groot, C. The Concurrent.Futures Library. *Asynchronous Program. with Python* (2020) doi:10.1007/978-1-4842-6582-6_12.

92. Hunter, J. D. Matplotlib: A 2D graphics environment. *Comput. Sci. Eng.* **9**, 90–95 (2007).

93. Image representation in Python — pyFAI 0.22.0a5 documentation. https://pyfai.readthedocs.io/en/master/geometry.html.

94. Li, H. X., Lu, Z. C., Wang, S. L., Wu, Y. & Lu, Z. P. Fe-based bulk metallic glasses: Glass formation, fabrication, properties and applications. *Prog. Mater. Sci.* **103**, 235–318 (2019).

95. Pan, J., Chen, Q., Li, N. & Liu, L. Formation of centimeter Fe-based bulk metallic glasses in low vacuum environment. *J. Alloys Compd.* **463**, 246–249 (2008).

96. Londoño-Restrepo, S. M., Jeronimo-Cruz, R., Millán-Malo, B. M., Rivera-Muñoz, E. M. & Rodriguez-García, M. E. Effect of the Nano Crystal Size on the X-ray Diffraction Patterns of Biogenic Hydroxyapatite from Human, Bovine, and Porcine Bones. *Sci. Reports 2019 91* **9**, 1–12 (2019).

97. Mukherjee, S., Zhou, Z., Schroers, J., Johnson, W. L. & Rhim, W. K. Overheating threshold and its effect on time–temperature-transformation diagrams of zirconium based bulk metallic glasses. *Appl. Phys. Lett.* **84**, 5010 (2004).

Appendix

Integration

In [28]:

```
import numpy as np
import matplotlib.pyplot as plt
from matplotlib.animation import FuncAnimation
import os
import time
import numpy
import pyFAI
import fabio
import concurrent.futures
from IPython.display import clear_output
```

In [29]:

```
'''GLOBAL VARIABLES'''


UNIT = 'q_nm^-1'

DELETE_OLD = False #Change to True if you want to delete the old files

data_points = 1000 # Datapoints for integration

poni_file = [i for i in os.listdir() if i.endswith(".poni")][0]
ai = pyFAI.load(poni_file)

all_cbf = [i for i in os.listdir() if i.startswith('FeBMG') if i.endswith('.cbf')] #Cha
nge this for other Files
all_cbf.sort()

print(os.getcwd())

all_files = os.listdir()
```

```
/home/jupyter-froemer/FeBMG/FeBMG02_h250_iso0p5_c10000_r1_pilatus
```

In [30]:

```
def Integration1D(one_file):
    '''1D Integration of one file and saves it'''
    destination = os.path.splitext(one_file)[0]+".txt"
    method=('1d int, no split, histogram, python')
    if os.path.exists(destination):
        pass
    else:
        clear_output(wait = True)
        img = fabio.open(one_file).data
        res = ai.integrate1d(img, data_points, unit=UNIT)
        np.savetxt(destination, res)
        clear_output(wait = True)
    return

def Multiprocessing(files):
    '''MULTIPROCESSING OF THE FILES WITH THE INTEGRATION1D FUNCTION'''
    with concurrent.futures.ProcessPoolExecutor() as executor:
        executor.map(Integration1D, files)
    return
```

In [26]:

```
##### Saves 1DIntegrationdata in .txt files#####
### ~25s for 1625 files ###

start_time = time.perf_counter()
def main():

    Multiprocessing(all_cbf)

    return

if __name__ == '__main__':

    main()

print(f"Total execution time: {time.perf_counter()-start_time:.3f} s")
```

Chip calibration and mask

In [1]:

```
import numpy as np
import matplotlib.pyplot as plt
from matplotlib.animation import FuncAnimation
import os
import time
import numpy
import pyFAI
import fabio
# import concurrent.futures
# import numpy as np
from pyFAI.gui import jupyter
# from matplotlib.pyplot import subplots
# import matplotlib.pyplot as plt
# from scipy.signal import find_peaks
# import json
# import warnings
from scipy.optimize import curve_fit
# import pickle
```

In [2]:

```
'''GLOBAL VARIABLES'''

UNIT = 'q_nm^-1'

data_points = 1000 # Datapoints for integration

poni_file = [i for i in os.listdir() if i.endswith(".poni")][0]
ai = pyFAI.load(poni_file)

print(os.getcwd())
```

```
/home/jupyter-froemer/FeBMG/FeBMG02_h250_iso0p5_c10000_r1_pilatus
```

In [3]:

```
DELETE_OLD = True
X_MIN = 5 # Exclude starting region
X_MAX = 20.5 # Exclude ending region
MIN_PEAK = 0.2 # Minimum Peak for masking
N = 0 #Show the measurement image of file numer N

start_time = time.perf_counter()
os.chdir(r'/home/jupyter-froemer/FeBMG/FeBMG02_h250_iso0p5_c10000_r1_pilatus/empty_chi
p')
all_files = os.listdir()
all_files.sort()
txt_destination = 'empty_cells_middled.txt'
method=('1d int, no split, histogram, python')

if DELETE_OLD == True:
    if os.path.exists(txt_destination):
        os.unlink(txt_destination)

cells_cbf = [i for i in all_files if i.startswith('empty_cell') if i.endswith('.cbf')]

Middled = np.zeros(data_points)

for cell in cells_cbf:
    if os.path.exists(txt_destination):
        pass
    else:

        img = fabio.open(cell).data
        unit, Intensity = ai.integrate1d(img, data_points, unit=UNIT)
        for n, _ in enumerate(Intensity):
            Intensity[n] = _ / len(cells_cbf)
        Middled+=Intensity
```

In [4]:

```
#jupyter.display(fabio.open(cells_cbf[N]).data, label=cells_cbf[N])
```

In [5]:

```
#####Uncommed for comparison between measured cell and middled data
unit, Intensity = ai.integrate1d(img, data_points, unit=UNIT)
plt.plot(unit, Intensity, label=cells_cbf[N])

plt.plot(unit, Middled, label ='Middled')
plt.legend()
plt.xlabel(UNIT)
plt.ylabel('Intensity')
```

Out[5]:

```
Text(0, 0.5, 'Intensity')
```

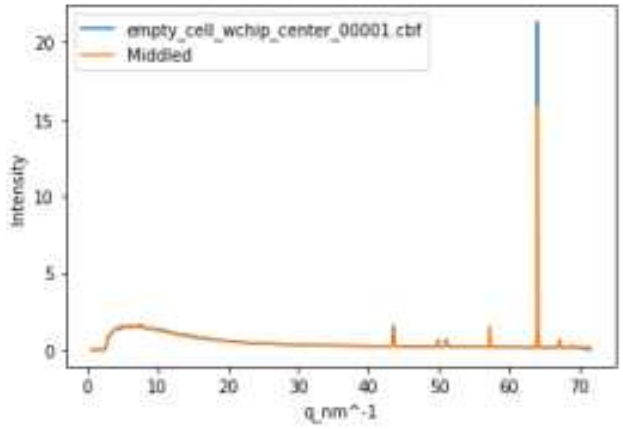

In [6]:

```
##### Subtract base line #####
##### Enter fixed x Coordinates for base line####
coordinates = [30,40,53,60]

x=[]
y=[]
for n,_ in enumerate(unit):
    for i in coordinates:
        if _ >= i:
            y.append(Intensity[n])
            x.append(unit[n])
            coordinates.remove(i)
print(y)
print(x)
plt.scatter(x, y, label='Points')
mymodel = numpy.poly1d(numpy.polyfit(x, y, 3))
plt.plot(unit, mymodel(unit),label ='Base line')
plt.plot(unit, Middled, label ='Middled')
plt.ylim(0,4)
plt.legend
plt.xlabel(UNIT)
plt.ylabel('Intensity')
```

```
[0.33749488, 0.24975954, 0.1897854, 0.17325471]
[30.04867847569701, 40.067962415239236, 53.00065515989659, 60.035471542979
43]
```

Out[6]:

```
Text(0, 0.5, 'Intensity')
```

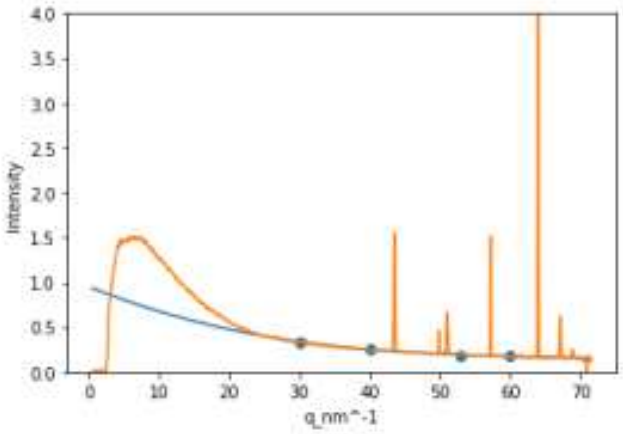

In [7]:

```
plt.plot(unit, Middled-mymodel(unit),label ='Middled without base line')
plt.ylim(0,4)
plt.legend
plt.xlabel(UNIT)
plt.ylabel('Intensity')
```

Out[7]:

```
Text(0, 0.5, 'Intensity')
```

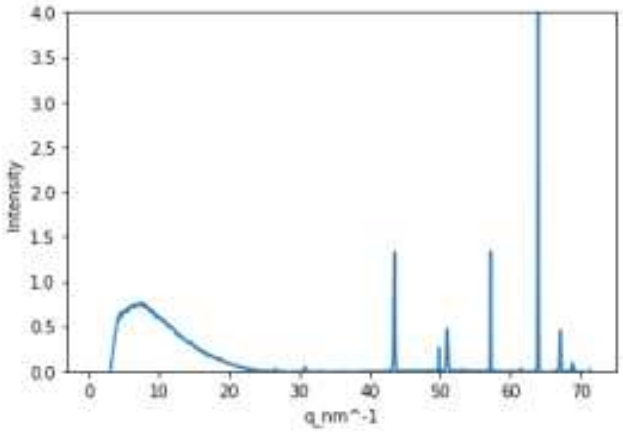

In [8]:

```
##### Filtering of Diffuse Background#####
XMIN = 0
XMAX = 24
YMIN = 0
x=unit
y=Middled-mymodel(unit)
xnew=[]
ynew=[]

for n,_ in enumerate(x):
    if _ >= XMIN and _<=XMAX and y[n]>0:
        xnew.append(x[n])
        ynew.append(y[n])
plt.plot(xnew,ynew)
plt.xlabel(UNIT)
plt.ylabel('Intensity')
```

Out[8]:

```
Text(0, 0.5, 'Intensity')
```

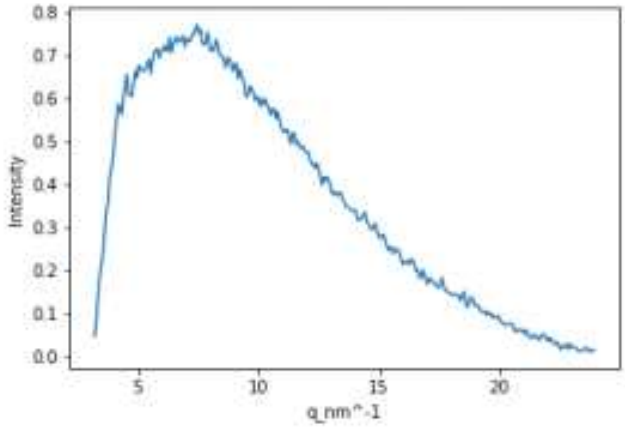

In [9]:

```
def polynominal(x, A, B, C, D, E,F,G):
    return A+B*x+C*x**2+D*x**3+E*x**4+F*x**5+G*x**6

coef, _ = curve_fit(polynominal, xnew,ynew)
A, B, C, D, E,F,G = coef
fittedY=[]
for _ in xnew:
    fittedY.append(A+B*_+C*_**2+D*_**3+E*_**4+F*_**5+G*_**6)
ynew = np.array(ynew)
# print(fitted_Y)
Y = np.array(ynew)-np.array(fittedY)

plt.plot(xnew,ynew, label ='Base line')
plt.plot(xnew, fittedY, label ='Spline')
# plt.ylim(0,4)
# plt.legend
plt.xlabel(UNIT)
plt.ylabel('Intensity')
```

Out[9]:

```
Text(0, 0.5, 'Intensity')
```

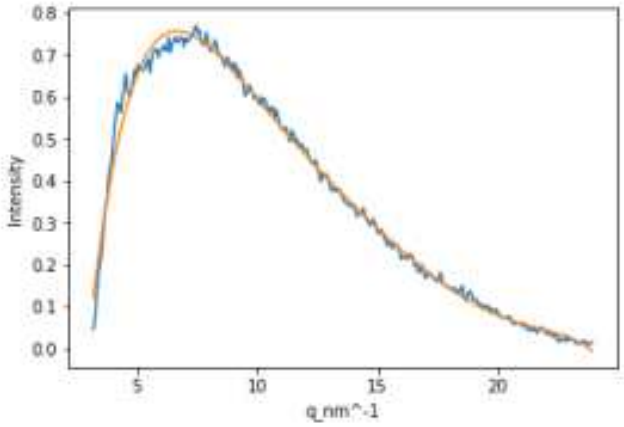

In [10]:

```
Y = Middled-mymodel(unit)
xnew = np.array(xnew)
MIN_PEAK=0.1

for n, _ in enumerate(ynew):
    Y[n]=Y[n]-ynew[n]
for n, _ in enumerate(Y):
    if _<0:
        Y[n]=0
plt.plot(unit,Y)
plt.xlabel(UNIT)
plt.ylabel('Intensity')
```

Out[10]:

```
Text(0, 0.5, 'Intensity')
```

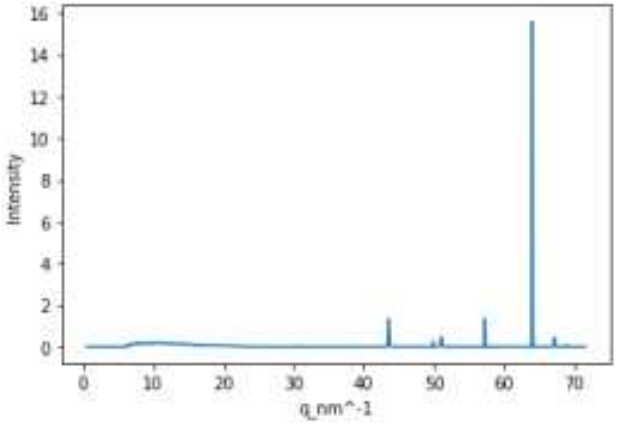

In [11]:

```
##### SET Line to Zero between these two Numbers
XMIN=0
XMAX=25
for n,_ in enumerate(unit):
    if _<=XMAX:
        Y[n]=0

plt.plot(unit,Y)
plt.xlabel(UNIT)
plt.ylabel('Intensity')
```

Out[11]:

```
Text(0, 0.5, 'Intensity')
```

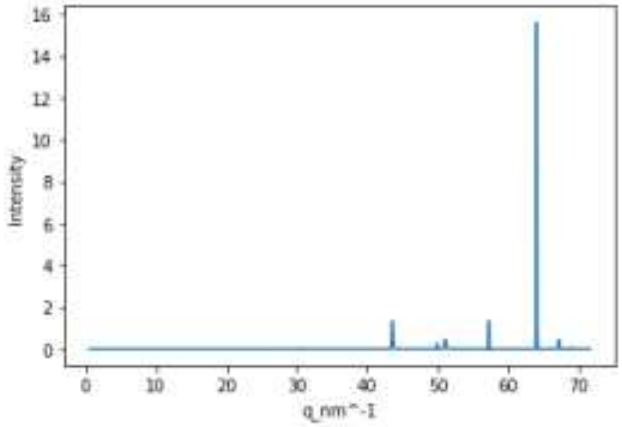

In [12]:

```
##### ALL PEAKS to height 1
Y_mask = Y*10 # For better filtering of the peaks
MIN_PEAK = 0.1
plt.plot(unit,Y+1.5) # For comparison
Y_mask = Y*10
for n,_ in enumerate(Y_mask):
    if _<=MIN_PEAK:
        Y_mask[n]=0
    if _>=MIN_PEAK:
        Y_mask[n]=1
plt.ylim(0,3)
plt.plot(unit,Y_mask)
mask=[]
for _ in Y_mask:
    if _ == 0:
        mask.append(True)
    if _ == 1:
        mask.append(False)
plt.xlabel(UNIT)
plt.ylabel('Intensity')
```

Out[12]:

```
Text(0, 0.5, 'Intensity')
```

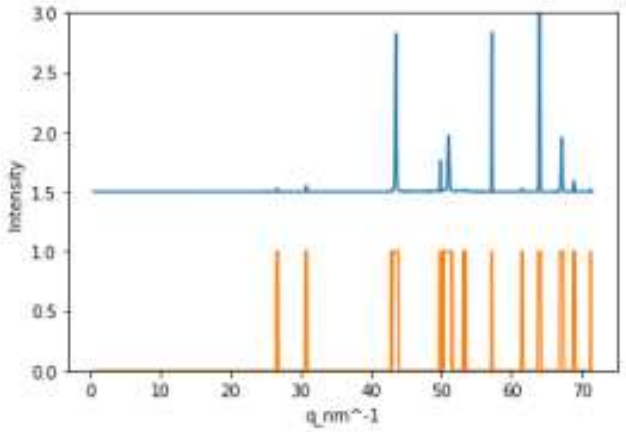

In [13]:

```
#### For Control! If no peaks bigger than MIN_PEAK are visible they are all filterd by
 the mask
plt.plot(unit[mask],Y[mask])
plt.xlabel(UNIT)
plt.ylabel('Intensity')
print('Min_PEAK',MIN_PEAK)
```

```
Min_PEAK 0.1
```

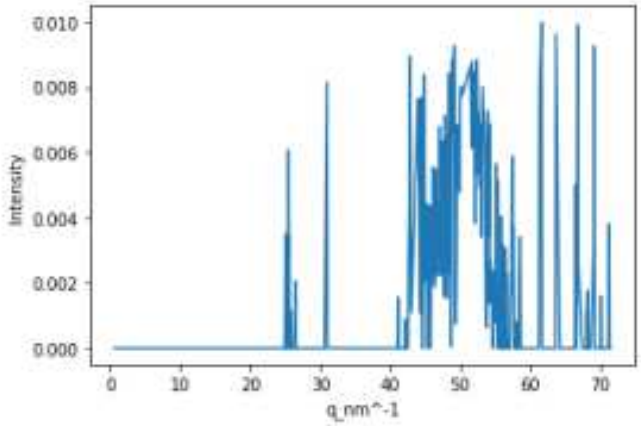

In [14]:

```
# For control if all chip peaks are masked!

plt.plot(unit[mask], Middled[mask])
#plt.title('Fully masked chip')
plt.yticks([])
plt.ylabel('Intensity [a.u.]')
plt.xlabel('q [nm$^{-1}$]')
```

Out[14]:

```
Text(0.5, 0, 'q [nm$^{-1}$]')
```

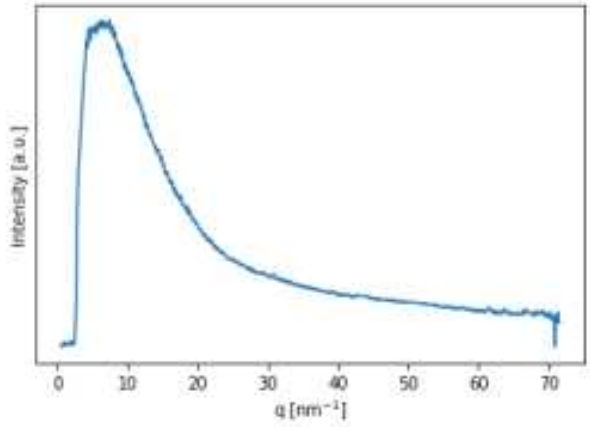

In [15]:

```
#### Save mask if not already existing
DELETE_OLD = True
MASK_DESTINATION = "mask.txt"
if DELETE_OLD == True:
    np.savetxt(MASK_DESTINATION, Y_mask)
    print('New mask saved!')
```

```
New mask saved!
```

Editing

In [1]:

```
import numpy as np
import matplotlib.pyplot as plt
from matplotlib.animation import FuncAnimation
import os

import numpy
import pyFAI
import fabio
```

In [2]:

```
'''GLOBAL VARIABLES'''

UNIT = 'q_nm^-1'

data_points = 1000 # Datapoints for integration

poni_file = [i for i in os.listdir() if i.endswith(".poni")][0]
ai = pyFAI.load(poni_file)

print(os.getcwd())
```

```
/home/jupyter-froemer/FeBMG/FeBMG02_h250_iso0p5_c10000_r1_pilatus
```

In [3]:

```
#### Load Mask ####
os.chdir(r'/home/jupyter-froemer/FeBMG/FeBMG02_h250_iso0p5_c10000_r1_pilatus/empty_chi
p')
all_files = os.listdir()
mask_txt = [i for i in all_files if i.startswith('mask') if i.endswith('.txt')]
mask=[]
with open(mask_txt[0]) as file:
    data = file.readlines()
for line in data:
    line.rstrip('\n')
    line = float(line)
    if line == 1:
        mask.append(False)
    if line == 0:
        mask.append(True)
os.chdir("..")
print('Mask loaded!')
```

```
Mask loaded!
```

In [4]:

```
### Integrates one file
N=1000
all_files = os.listdir()
all_cbf = [i for i in all_files if i.startswith('FeBMG') if i.endswith('.cbf')]
all_cbf.sort()
img = fabio.open(all_cbf[N]).data
res = ai.integrate1d(img, data_points, unit=UNIT)


x= res[0]
x_mask = x
y= res[1]

x_masked=x[mask]
y_masked=y[mask]
plt.plot(x[mask],y[mask], label= 'masked')
plt.plot(x,y+2, label= 'measured')
plt.plot(x_mask,data, label= 'mask')
plt.legend()
plt.ylabel('Intensity [a.u.]')
plt.xlabel('q [nm$^{-1}$]')
plt.yticks([])
plt.ylim(0,4)
plt.title(all_cbf[N])
```

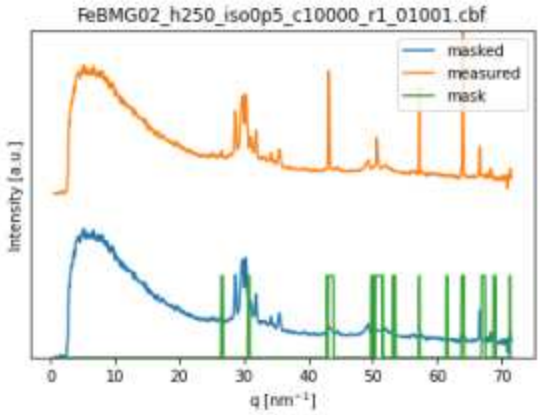

In [5]:

```
##### Subtract base line #####
##### Enter fixed x Coordinates for base line####
coordinates = [23,40,46,60,65]
coordinates_fix = coordinates
x_points=[]
y_points=[]
for n,_ in enumerate(x_masked):
    for i in coordinates:
        if _ >= i:
            y_points.append(y_masked[n])
            x_points.append(x_masked[n])
            coordinates.remove(i)

plt.scatter(x_points, y_points, label='Points')
plt.title(all_cbf[N])
mymodel = numpy.poly1d(numpy.polyfit(x_points, y_points, 3))
plt.plot(x_masked, mymodel(x_masked),label ='Baseline')
plt.plot(x_masked, y_masked, label ='Masked')
plt.ylim(0,4)
plt.legend()
plt.ylabel('Intensity [a.u.]')
plt.xlabel('q [nm$^{-1}$]')
```

Out[5]:

```
Text(0.5, 0, 'q [nm$^{-1}$]')
```

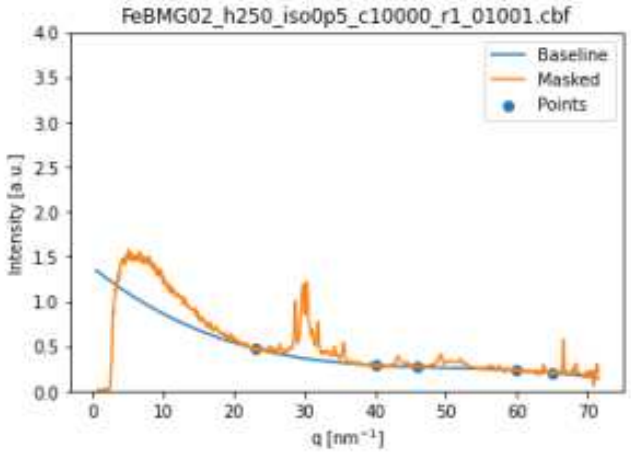

In [6]:

```
##### Set every value to zero below the first coordinate #####
XMAX = 24

x = x_masked
print(len(x))
y = y_masked-mymodel(x_masked)
for n,_ in enumerate(x):
    if _<=XMAX:
        y[n]=0
plt.plot(x, y,label ='Without base line')
plt.legend
plt.title(all_cbf[N])
plt.ylabel('Intensity [a.u.]')
plt.xlabel('q [nm$^{-1}$]')
plt.xlim(24,70)
```

```
929
```

Out[6]:

```
(24.0, 70.0)
```

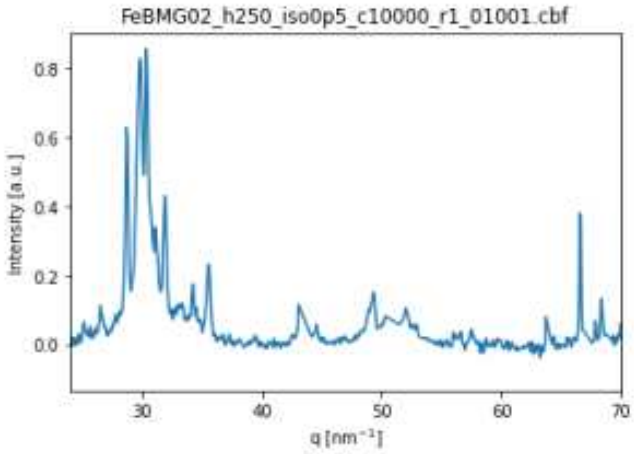

In [8]:

```
##### Additional masking#####
MINPEAK = 0
for n, _ in enumerate(y):
    if x[n]<XMAX:
        y[n]=0
    if y[n] < MINPEAK:
        y[n] = 0
plt.plot(x,y)
plt.title(all_cbf[N])
plt.ylabel('Intensity [a.u.]')
plt.xlabel('q [nm$^{-1}$]')
plt.xlim(24,70)
plt.plot(x_mask,data, label= 'mask', alpha =0.5)
plt.yticks([])
x1=26
x2=27
plt.axvline(x1,color = 'r')
plt.axvline(x2,color = 'r')
x3=30.5
x4=31.3
plt.axvline(x3,color = 'r')
plt.axvline(x4,color = 'r')
x5=42.7
x6=44
plt.axvline(x5,color = 'r')
plt.axvline(x6,color = 'r')
x7=57
x8=58
plt.axvline(x7,color = 'r')
plt.axvline(x8,color = 'r')
x9=63
x10=64
plt.axvline(x9,color = 'r')
plt.axvline(x10,color = 'r')
x11=65
x12=67
plt.axvline(x11,color = 'r')
plt.axvline(x12,color = 'r')
x13=68
x14=69
plt.axvline(x13,color = 'r')
plt.axvline(x14,color = 'r')
for n,_ in enumerate(x):
    if _>x1 and _<x2:
        mask_2[n]=False
for n,_ in enumerate(x):
    if _>x3 and _<x4:
        mask_2[n]=False
for n,_ in enumerate(x):
    if _>x5 and _<x6:
        mask_2[n]=False
for n,_ in enumerate(x):
    if _>x7 and _<x8:
        mask_2[n]=False
for n,_ in enumerate(x):
    if _>x9 and _<x10:
        mask_2[n]=False
for n,_ in enumerate(x):
    if _>x11 and _<x12:
```

```
        mask_2[n]=False
for n,_ in enumerate(x):
    if _>x13 and _<x14:
        mask_2[n]=False
```

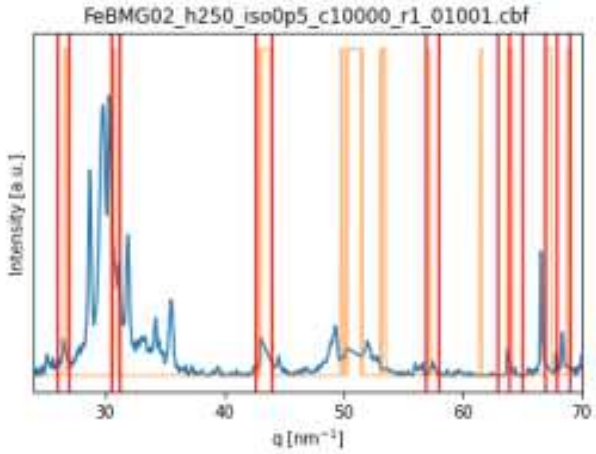

In [9]:

```
x=res[0]
print(len(x))
y=res[1]
print(len(y))
new_mask = [True]*len(res[0])
for n,_ in enumerate(mask):
    if _ == False:
        new_mask[n] = False
for n,_ in enumerate(mask_2):
    if _ == False:
        new_mask[n] = False
plt.plot(x[new_mask],y[new_mask])
plt.title(all_cbf[N])
plt.ylabel('Intensity [a.u.]')
plt.xlabel('q [nm$^{-1}$]')
plt.xlim(24,70)
plt.plot(x_mask,data, label= 'mask', alpha =0.5)
plt.yticks([])
```

```
1000
1000
```

Out[9]:

```
([], [])
```

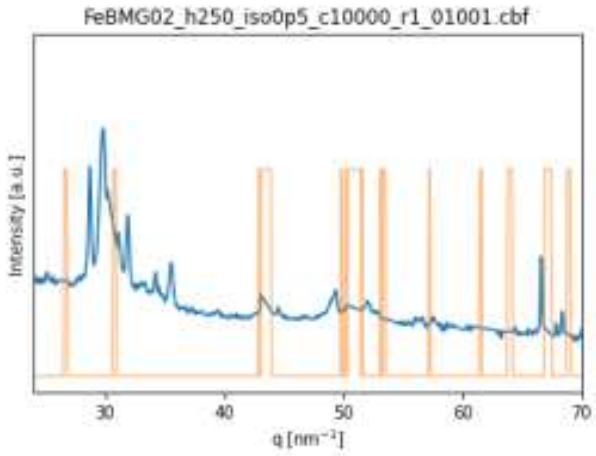

In [11]:

```
### Integrates one file
N=1000
all_files = os.listdir()
all_cbf = [i for i in all_files if i.startswith('FeBMG') if i.endswith('.cbf')]
all_cbf.sort()
img = fabio.open(all_cbf[N]).data
res = ai.integrate1d(img, data_points, unit=UNIT)


x= res[0]
y= res[1]
x_masked=x[new_mask]
y_masked=y[new_mask]
plt.plot(x_masked,y_masked, label= 'masked')
plt.plot(x,y+2, label= 'measured')

plt.legend()
plt.ylabel('Intensity [a.u.]')
plt.xlabel('q [nm$^{-1}$]')
plt.yticks([])
plt.ylim(0,6)
plt.title(all_cbf[N])
```

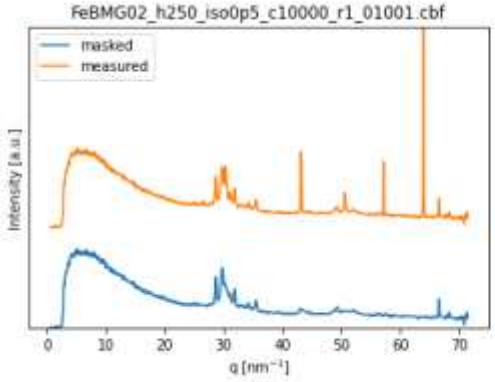

In [12]:

```
##### SAVE MASK #####
os.chdir(r'/home/jupyter-froemer/FeBMG/FeBMG02_h250_iso0p5_c10000_r1_pilatus/empty_chi
p')
MASK_DESTINATION = "mask.txt"
np.savetxt(MASK_DESTINATION, mask)
print('Mask saved!')
os.chdir("..")
```

```
Mask saved!
```

Final preparation

In [4]:

```
import numpy as np
import matplotlib.pyplot as plt
from matplotlib.animation import FuncAnimation
import os
import time
import numpy
import pyFAI
import fabio
import concurrent.futures
```

In [5]:

```
def Multiprocessing_final(alltxt):
    '''MULTIPROCESSING OF THE FILES WITH A FUNCTION'''
    with concurrent.futures.ProcessPoolExecutor() as executor:
        executor.map(Final_preparation, alltxt)
    return
def Final_preparation(one_txt):
    '''Final preparation like all above'''
    coordinates = [23,40,47,60,65]
    XMAX= 22
    MINPEAK = 0.01
    destination = os.path.splitext(one_txt)[0]+"_final.txt"
    if os.path.exists(destination):
        pass
    else:
        #### Load Mask ####
        os.chdir(r'/home/jupyter-froemer/FeBMG/FeBMG02_h250_iso0p5_c10000_r1_pilatus/em
pty_chip')
        all_files = os.listdir()
        mask_txt = [i for i in all_files if i.startswith('mask') if i.endswith('.txt')]
        mask=[]
        with open(mask_txt[0]) as file:
            data = file.readlines()
        for line in data:
            line.rstrip('\n')
            line = float(line)
            if line == 1:
                mask.append(True)
            if line == 0:
                mask.append(False)
        os.chdir("..")

    ####Opens a .txt file and returns reduced x and y values'''
        txt = np.loadtxt(one_txt)
        x= txt[0]
        y= txt[1]
        for n,_ in enumerate(y):
            if np.isnan(_):
                y[n]=0

        x_masked=x[mask]
        y_masked=y[mask]
#         plt.plot(x_masked,y_masked)
#         plt.show()

    ##### Subtract base line #####

        x=[]
        y=[]
        for n,_ in enumerate(x_masked):
            for i in coordinates:
                if _ >= i:
                    y.append(y_masked[n])
                    x.append(x_masked[n])
                    coordinates.remove(i)

        #plt.scatter(x, y, label='Points')
        mymodel = numpy.poly1d(numpy.polyfit(x, y, 3))

        x = x_masked
```

```
        y= y_masked-mymodel(x_masked)

    ##### Filtering of Diffuse Background by x_max and min peak#####

        for n, _ in enumerate(y):
            if x[n]<XMAX:
                y[n]=0
            if y[n] < MINPEAK:
                y[n] = 0
        res = [x,y]

        np.savetxt(destination, res)
    return

def open_txt_file(file):

    '''Opens a .txt file and returns reduced x and y values'''

    if file.endswith('.txt'):
        txt = np.loadtxt(file)
        x= txt[0]
        y= txt[1]
        for n,_ in enumerate(y):
            if np.isnan(_):
                y[n]=0

        return x, y
```

In [6]:

```
##### Saves Final data in final.txt files #####

all_files = os.listdir()
all_txt = [i for i in all_files if i.startswith('FeBMG') if i.endswith('.txt') if not
'final' in i]
all_txt.sort()

####Delete all final.txt
DELETE_OLD = True
all_files = os.listdir()
if DELETE_OLD == True:
    for one_file in all_files:
        if one_file.endswith('final.txt'):
            os.unlink(one_file)

def main():

    Multiprocessing_final(all_txt)

    return

if __name__ == '__main__':

    start_time = time.perf_counter()

    main()
```

In [7]:

```
##### Investigation of a final file#####
N=1400
all_files = os.listdir()
all_measurements = [i for i in all_files if i.endswith(".txt") if i.startswith("FeBMG")
if not i.endswith("final.txt") ]
all_final = [i for i in all_files if i.endswith("_final.txt") if i.startswith("FeBMG")]
all_measurements.sort()
all_final.sort()
file = all_measurements[N]
q, I = open_txt_file(file)
plt.plot(q,I, label = 'measured')
file = all_final[N]
q, I = open_txt_file(file)

plt.plot(q,I+5, label = 'final')
plt.ylabel('Intensity [a.u.]')
plt.xlabel('q [nm$^{-1}$]')
plt.yticks([])
plt.title(N)
#plt.plot(unit,test, label ='mask'  )
```

Out[7]:

```
Text(0.5, 1.0, '1400')
```

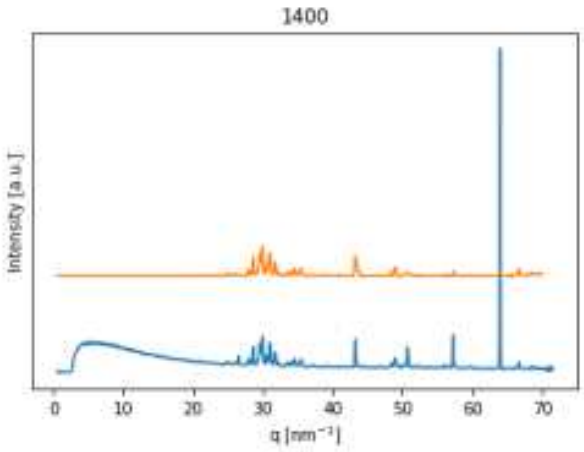

Temperature measurement

In [1]:

```
import numpy as np
import matplotlib.pyplot as plt
from matplotlib.animation import FuncAnimation
import os
import time
import numpy
import pyFAI
import fabio

all_files = os.listdir()
all_measurements = [i for i in all_files if i.endswith(".txt") if i.startswith("FeBMG")
if not i.endswith("final.txt") ]
```

In [2]:

```
def open_txt_file(file):

    '''Opens a .txt file and returns reduced x and y values'''

    if file.endswith('.txt'):
        txt = np.loadtxt(file)
        x= txt[0]
        y= txt[1]
        for n,_ in enumerate(y):
            if np.isnan(_):
                y[n]=0

        return x, y
```

In [3]:

```
#### Choose one peak for temperature investigation
######for q
YMIN=30
YMAX=31
######for r
#YMIN=110
#YMAX=117
q_new=[]
I_new=[]
q, I = open_txt_file(all_measurements[0])
plt.plot(q,I)
for n,_ in enumerate(q):
    if _>YMIN and _<YMAX:
        q_new.append(_)
        I_new.append(I[n])

plt.plot(q_new,I_new)
plt.ylabel('Intensity [a.u.]')
plt.xlabel('q [nm$^{-1}$]')
plt.savefig('one_peak.png')
```

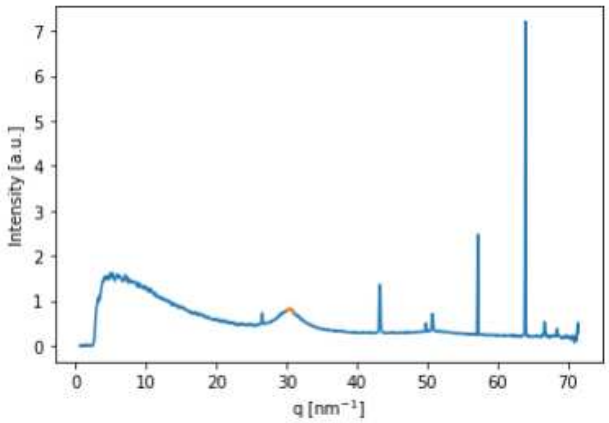

In [7]:

```
##### Choosing the startframe of the cooling phase
YMIN=42.5
YMAX=44.5
Intensity2D = []
for file in all_measurements:
    q_new=[]
    I_new=[]
    q, I = open_txt_file(file)
    for n,_ in enumerate(q):
        if _>YMIN and _<YMAX:
            q_new.append(_)
            I_new.append(I[n])
    Intensity2D.append(I_new)
Intensity2D=np.array(Intensity2D)
Intensity2D=Intensity2D.transpose()

x = np.linspace(1,len(all_measurements)+1, num=len(all_measurements))
x_grid=np.arange(min(x),max(x),len(x)/len(all_measurements))
y_grid=np.arange(min(q_new),max(q_new),(max(q_new)-min(q_new))/len(q_new))

plt.contourf(x_grid,y_grid,Intensity2D,100, vmin=0,vmax=2,cmap="jet")
cbar = plt.colorbar()
cbar.set_label('Intensity', rotation=90)
plt.xlabel('Frames')

plt.ylabel('q [nm$^{-1}$]')

##### Uncommend for closer view
#plt.xlim(1386,1400)
#plt.ylim(42.75,43.50)

##### Choose the start of the cooling phase #####
Coolingstart= 1388
plt.axvline(Coolingstart,color = 'r')
```

Out[7]:

```
<matplotlib.lines.Line2D at 0x7f45326e4160>
```

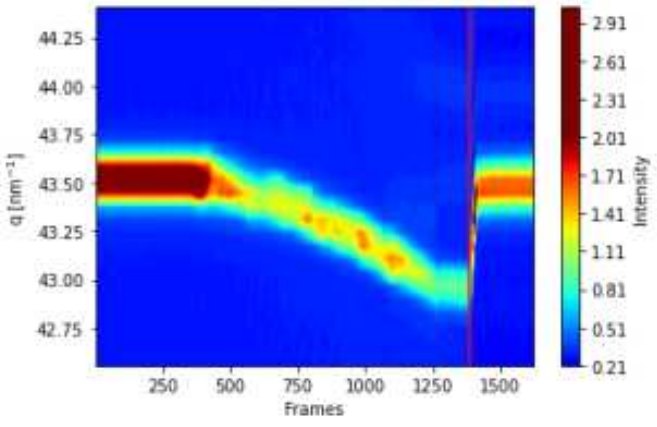

In [12]:

```
##### ideal temperature profile #####
Tr = 29
Tmax = 950
iso1 = 1 # [s]
iso2 = 0.5 # [s]
Heatingrate = 250 # [K/s]
Coolingrate = 10000 # [K/s]
Framerate = 250 # Frames/s

x = np.linspace(1,len(all_measurements)+1, num=len(all_measurements))
t= np.linspace(1/Framerate,(int(max(x))-1)/Framerate,(int(max(x))-1))
T=[]
Tx = 0
t1 = 0
t2 = 0
n=0
for _ in t:
    if _ <= iso1:
        T.append(Tr)
    if _ >= iso1 and Tx <= Tmax:
        Tx = Tr + Heatingrate * (_ - iso1)
        T.append(Tx)
        t1 = _
    if _ - iso1 -t1 >= 0 and _ - iso1 -t1 <= iso2:
        T.append(Tmax)
    if _ - iso1 -t1 >= iso2 and Tx >= Tr:
        Tx = Tmax - Coolingrate * (_ - iso1 -t1-iso2)
        T.append(Tx)
while len(T)<= len(t)-1:
    T.append(Tr)

for n, _ in enumerate(T):
    if _ > Tmax:
        T[n]=Tmax


##### Real Temperature Profile with fixed point at the start of the cooling #####


t0 = Coolingstart/Framerate
t= np.linspace(1/Framerate,(int(max(x))-1)/Framerate,(int(max(x))-1))
th = (Tmax-Tr)/Heatingrate
tc= (Tmax-Tr)/Coolingrate
Treal=[]
for _ in t:
    if _ <= t0-iso2-th: # Iso before heating
        Treal.append(Tr)
    if _ > t0-iso2-th and _ <= t0-iso2: # Heating
        Treal.append(Tr+Heatingrate* abs(_-(t0-iso2-th)))
    if _ > t0-iso2 and _ <= t0: # Iso at high temperature
        Treal.append(Tmax)
    if _ > t0 and _ <= t0+tc: # Cooling
        if Tmax-Coolingrate*abs(t0-_)>Tr:
            Treal.append(Tmax-Coolingrate*abs(t0-_))
    if _ > t0+tc: # Iso after cooling
        Treal.append(Tr)

plt.plot(t,Treal, label = 'real')
plt.plot(t,T, label = 'theoretical')
```

```
plt.xlabel('Time [s]')
plt.ylabel('Temperature [°C]')
plt.legend()

##### Calculation of Delta T
k=[]
x=[]

for n, _ in enumerate(T):
    if _ > 400:
        k.append(n)

for n, _ in enumerate(Treal):
    if _ > 400:
        x.append(n)

deltaT = abs(t[k[0]]-t[x[0]])
print('DeltaT =',deltaT,'[s]')
res = [t,Treal]

##### SAVING ######
destination = 'Temperature.txt'
np.savetxt(destination, res)
print('Temperature profile saved!')
```

```
DeltaT = 0.3599999999999999 [s]
Temperature profile saved!
```

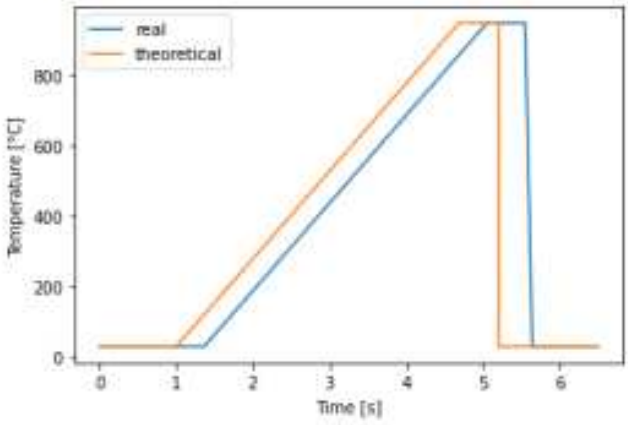

Intensitymap

In [2]:

```
import numpy as np
import matplotlib.pyplot as plt
from matplotlib.animation import FuncAnimation
import os
import time
```

In [3]:

```
def open_txt_file(file):

    '''Opens a .txt file and returns reduced x and y values'''

    if file.endswith('.txt'):
        txt = np.loadtxt(file)
        x= txt[0]
        y= txt[1]
        for n,_ in enumerate(y):
            if np.isnan(_):
                y[n]=0

        return x, y
```

In [8]:

```
'''Produces an Intensity map with all the _final.txt in the directory'''
start_time = time.perf_counter()

all_files = os.listdir()
Intensity2D = []
all_measurements = [i for i in all_files if i.endswith("final.txt") if i.startswith("Fe
BMG") ]
all_measurements.sort()
Tfile = [j for j in all_files if j.endswith(".txt") if j.startswith("T") ]
Tfile=Tfile[0]
t,Treal = open_txt_file(Tfile)
x = np.linspace(1,len(all_measurements)+1, num=len(all_measurements))
for file in all_measurements:
    q, I = open_txt_file(file)
    for m,z in enumerate(q):
        if z>42.5 and z<44:
            I[m]=0
        if z>66 and z<67.5:
            I[m]=0
        if z>50 and z<51:
            I[m]=0
    Intensity2D.append(I)
Intensity2D=np.array(Intensity2D)
Intensity2D=Intensity2D.transpose()
x_grid=np.arange(min(x),max(x),len(x)/len(all_measurements))
y_grid=np.arange(0,max(q),max(q)/len(q))

plt.subplot(3,5,(1,10) )
plt.contourf(x_grid,y_grid,Intensity2D,100, vmin=0,vmax=2,cmap="jet")
cbar = plt.colorbar()
cbar.set_label('Intensity', rotation=90)
plt.xticks([])
plt.ylabel('q [nm$^{-1}$]')

plt.subplot(3,5,(11,14) )
plt.plot(t,Treal)
plt.xlim(0,max(t))
plt.ylim(0,max(Treal)*1.1)
plt.ylabel('Temperature [°C]')
plt.yticks(np.arange(0, 1100, step=200))
plt.xlabel('Time [s]')
plt.subplots_adjust(bottom=0,
                    left=0.025,
                    top = 0.975,
                    right=0.975)
plt.grid()


print(f"Total execution time: {time.perf_counter()-start_time:.3f} s")
```

```
Total execution time: 9.595 s
```